Integrability Breaking and Bound States in Google's Decorated XXZ Circuits

Ana Hudomal[1,2] Ryan Smith,[1] Andrew Hallam,[1] and Zlatko Papić[1,*]

[1]*School of Physics and Astronomy, University of Leeds, Leeds LS2 9JT, United Kingdom*
[2]*Institute of Physics Belgrade, University of Belgrade, Belgrade 11080, Serbia*

Recent quantum simulation by Google [Nature **612**, 240 (2022)] has demonstrated the formation of bound states of interacting photons in a quantum-circuit version of the XXZ spin chain. While such bound states are protected by integrability in a one-dimensional chain, the experiment found the bound states to be unexpectedly robust when integrability was broken by decorating the circuit with additional qubits, at least for small numbers of qubits (≤ 24) within the experimental capability. Here we scrutinize this result by state-of-the-art classical simulations, which greatly exceed the experimental system sizes and provide a benchmark for future studies in larger circuits. We find that the bound states consisting of a *finite* number of photons are indeed robust in the nonintegrable regime, even after scaling to the infinite-time and infinite-system size limit. Moreover, we show that such systems possess unusual spectral properties, with level statistics that deviates from the random matrix theory expectation. On the other hand, for low but finite density of photons, we find a much faster onset of thermalization and significantly weaker signatures of bound states, suggesting that anomalous dynamics may only be a property of dilute systems with *zero* density of photons in the thermodynamic limit. The robustness of the bound states is also influenced by the number of decoration qubits and, to a lesser degree, by the regularity of their spatial arrangement.

I. INTRODUCTION

Recent advances in quantum simulators based on ultracold atoms, trapped ions, and superconducting circuits [1–8] have opened a window to studying far-from-equilibrium dynamics and thermalization in isolated many-body systems [9–12]. The behavior of generic thermalizing systems is described by the eigenstate thermalization hypothesis (ETH) [13–15], which seeks to explain the process of thermalization at the level of the system's energy eigenstates. In certain systems, the ETH can break down, allowing for new types of dynamical behavior and phases of matter to emerge [16]. One of the most striking manifestations of ergodicity breakdown occurs in finely tuned one-dimensional systems [17], which fail to thermalize due to their rich symmetry structure known as quantum integrability [18,19].

A paradigmatic quantum integrable system is the spin-1/2 XXZ model, which describes the low-energy physics of certain ferromagnetic materials [20]. In one spatial dimension, the model's *tour de force* analytic solution in the isotropic limit was presented by Bethe in the 1930s [21]. One remarkable consequence of that solution was a special class of eigenstates that can be viewed as bound states of magnons—the elementary quasiparticle excitations, whose signatures were observed in spectroscopic experiments [22–24]. However, due to the challenges of probing bound states via conventional techniques such as inelastic neutron scattering, it has been proposed [25] that local quenches [26–32] may provide deeper insight into the physics of bound states [33–39]. Dynamical signatures of bound states were indeed observed in systems of ^{87}Rb atoms in an optical lattice, realizing an effective Heisenberg model [40].

While previous studies mostly focused on systems with continuous dynamics governed by a static Hamiltonian, it is also possible to construct equivalent Floquet models defined as a product of unitary matrices. Such models, whose quantum dynamics is intrinsically discrete, are better suited for quantum devices, which operate as a sequence of unitary gates. Quantum circuit models that correspond to the spin-1/2 Heisenberg model in the high-frequency limit were studied in Refs. [41,42]. Remarkably, the Floquet circuit realization was shown to be integrable for arbitrary parameters and not only in the small time-step limit where it reduces via Troterrization to the Hamiltonian model [41–43].

The Floquet XXZ model was recently experimentally realized using a ring of superconducting qubits connected by high-fidelity fSim quantum logic gates [44]. These qubits interact with each other by superconducting currents and can host excitations in the form of trapped photons. This setup has allowed for the preparation and observation of bound states of a few interacting photons, which were predicted and analytically studied in Ref. [45]. One of the advantages was the possibility of controllably breaking the integrability by attaching extra qubits to the main chain and thus changing the geometry of the system. In contrast with the expectation that the bound states are protected by integrability, it was experimentally observed that these states survive even in the non-integrable regime, as previously suggested for the Hamiltonian version of the model [25]. However, the robustness of the bound states was not studied in detail and the question of which mechanism protects it in the nonintegrable case remains open.

In this work, we use classical simulations, based on exact diagonalization (ED) and matrix product states (MPS), to gain understanding of the experiment in Ref. [44]. Specifically, we study the statistical properties of the Floquet spectrum in order to detect the transition from the integrable to the nonintegrable regime. We also employ time-evolving block decimation (TEBD) simulations to investigate the evolution of bound states and their robustness. In this way, we are able to reach far larger system sizes, photon numbers, and timescales compared to the quantum hardware [44]. In contrast to the experiment, which has limitations due to the unwanted leakage of photons, the photon number is conserved in our study. We find that sectors with *small but fixed* photon number have nonthermalizing spectral properties, which affect both their level statistics and quantum dynamics. Additionally, we confirm the experimental finding that the bound states in these sectors persist beyond the integrable regime. While this effect is pronounced in dilute systems containing small photon numbers, it appears to be restricted to *zero density* of excitations in the thermodynamic limit. By contrast, sectors with small but finite excitation density are found to thermalize rapidly as the photon number is increased, in parallel with the fast decay of bound states.

The remainder of this paper is organized as follows. In Sec. II we introduce the Floquet XXZ model that will be the main object of our study. In Sec. III we identify anomalous properties in the statistics of the Floquet quasienergy levels, including the average ratio of consecutive gaps and the density of states. These results are complemented by the spectral form factor, which captures the signatures of anomalous spectral features at an intermediate Thouless time scale, relevant to transport. In Sec. IV we study the evolution of bound states and their robustness to integrability breaking. We perform extrapolations to infinite system size and compare the data against the diagonal ensemble predictions, which provides information about

the *infinite-time* limit. In Sec. V we discuss several cases beyond those studied in experiment, in particular systems with a constant filling factor and different decoration patterns, including nonsymmetric ones. We summarize our results and discuss their implications in Sec. VI. Appendices provide more details about the corresponding continuous XXZ model, effects of different parameters, the origin of peaks in the density of states, and the properties of Floquet modes, such as their localization in the Fock space.

II. MODEL

The experiment in Ref. [44] realized a decorated ring of superconducting qubits, schematically illustrated in Fig. 1(a). If the occupancy is limited to zero or one photon per qubit, the photons can be modeled as hard-core bosons. Since we are considering a ring of qubits, we will impose periodic boundary conditions (PBCs) in our ED calculations, unless stated otherwise. The fundamental building block of the circuit is a two-qubit fSim gate acting on pairs of adjacent qubits,

$$\mathrm{fSim}(\theta, \phi, \beta) = \begin{pmatrix} 1 & 0 & 0 & 0 \\ 0 & \cos\theta & ie^{i\beta}\sin\theta & 0 \\ 0 & ie^{-i\beta}\sin\theta & \cos\theta & 0 \\ 0 & 0 & 0 & e^{i\phi} \end{pmatrix}, \quad (1)$$

where θ and β determine the nearest-neighbor hopping amplitude and phase, while ϕ represents the strength of interactions between neighboring qubits. The parameter β mimics the external magnetic flux threading the ring. In the following, we will primarily consider the case $\mathrm{fSim}(\theta, \phi, \beta = 0) = \mathrm{fSim}(\theta, \phi)$.

Figure 1(a) is a sketch of the model with decorations attached to every other site as in Ref. [44]. The number of photons will be denoted by N and the total number of sites by $L = L_{\mathrm{sites}} + L_{\mathrm{decor}}$, which includes both the sites
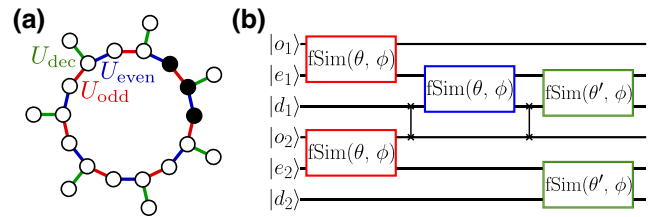

FIG. 1. (a) Sketch of the XXZ circuit model with $L = 14 + 7$ sites (7 unit cells). Filled dots denote a bound state of $N = 3$ photons. Here, the integrability-breaking decorations are attached to every other site. (b) An example of the corresponding quantum circuit with $L = 4 + 2$ sites. The circuit consists of fSim (boxes) and SWAP gates (vertical lines). The alternating layers of gates acting on even or odd bonds and decorations are denoted by blue, red, and green color, respectively, matching the unitaries U_{even}, U_{odd}, and U_{dec} in (a). Our classical MPS simulations in iTensor [46] follow this diagram and assume open boundary conditions.

on the ring L_{sites} and the extra sites L_{decor}. The sketch also depicts a state with $N = 3$ adjacent photons, which will typically be used as the initial state in our simulations. Note that there is another, similar configuration of three adjacent photons, that is simply shifted by one lattice site. This configuration is inequivalent to the one in Fig. 1(a) because it is connected to two decorations instead of one. As specified below, we will occasionally find it useful to average the results over these two initial states. In addition to the layout shown here, in Sec. V we will also consider other decoration patterns. In general, we find the dynamical properties are highly sensitive to the number of photons and the decoration pattern.

Figure 1(b) shows the corresponding quantum circuit, which consists of fSim and SWAP gates. The states of the even, odd, and decoration qubits are denoted by $|e_i\rangle$, $|o_i\rangle$, and $|d_i\rangle$, respectively. Our classical TEBD simulations follow the layout in Fig. 1(b) and, for convenience, assume open boundary conditions (OBCs). We emphasize that the results below are insensitive to the choice of boundary conditions, as we will demonstrate good agreement between TEBD with OBCs and ED with PBCs. The circuit is defined by first applying fSim gates across all odd bonds, then across all even bonds. Since the even and odd bonds are thus not equivalent, the system is invariant to translation by two lattice sites of the main chain. Additional gates which couple to the integrability-breaking extra sites $|d_i\rangle$ are subsequently applied, which can further reduce the symmetry of the full system depending on the pattern of arrangement of the extra sites. The coupling parameter θ' is used to tune between the integrable and nonintegrable regimes, while the interaction strength $\phi = \phi'$ is the same, both along the main chain and between the chain and the decorations. The one-cycle unitary operator is then

$$\hat{U}_F = \underbrace{\prod_{\text{extra bonds}} \text{fSim}(\theta', \phi)}_{\hat{U}_{\text{dec}}}$$

$$\times \underbrace{\prod_{\text{even bonds}} \text{fSim}(\theta, \phi)}_{\hat{U}_{\text{even}}} \underbrace{\prod_{\text{odd bonds}} \text{fSim}(\theta, \phi)}_{\hat{U}_{\text{odd}}}. \quad (2)$$

As shown in Appendix A, the Hamiltonian of the XXZ model corresponds to the Trotter-Suzuki expansion of this unitary in the $\phi, \theta, \theta' \to 0$ limit.

The isotropic XXX version of the model in Eq. (2) was first proposed in Ref. [41], while the Floquet XXZ model was formulated in Ref. [42] and analytically studied in detail in Ref. [45]. The latter used the Bethe ansatz to derive the dispersion of bound states containing an arbitrary number of photons. These bound states are formed by stable magnon quasiparticles, and there are two different phases depending on the ratio of θ and ϕ: (1) gapped phase

$\phi > 2\theta$, where bound states of any photon number exist for any momentum, and (2) gapless phase $\phi < 2\theta$ where the bound states are only present for a finite range of momenta. The maximal group velocity was found to decrease with the number of photons in the bound state. Quantum simulations [44] have later confirmed the analytical relations between the velocity of quasiparticles and their momentum. However, analytical solutions are not available for the nonintegrable case, where the integrability is broken either by adding certain perturbations or by changing the geometry of the system. We will use classical simulations to numerically study this regime.

A. Circular orthogonal ensemble

Before we analyze in detail the Floquet spectrum of Eq. (2), we must understand the relevant symmetries of the model as they affect the random matrix theory ensemble describing the spectrum after breaking the integrability [47]. For example, the undecorated model with PBCs is invariant under translation by two sites, due to the even and odd layers of fSim gates being applied separately. Such a circuit is also invariant under spatial inversion. However, attaching extra qubits to some of the sites reduces the symmetry of the full system. Regular patterns with decorations on every nth site will preserve some form of translation invariance, although with a larger unit cell. Furthermore, the system can be inversion symmetric only if the decoration pattern itself is also inversion symmetric. However, in some cases, such as that with decorations on every other site, the inversion of the decorations can be incompatible with the inversion of the main ring due to different reflection axes, so the full system only has translation symmetry, even though the decoration pattern is still inversion-symmetric. This will be discussed in more detail in Sec. V B.

For a general unitary matrix $\hat{U}_F$, the level statistics is expected to conform with the circular unitary ensemble (CUE). However, as will be apparent in Secs. III A and V B, in most cases studied here we obtain the circular orthogonal ensemble (COE) statistics instead. COE would trivially ensue if $\hat{U}_F = \hat{U}_F^T$, however this is not the case here for any arrangement of decorations. Our calculations show that the necessary conditions for COE level statistics are an inversion-symmetric decoration pattern and equal parameters for the fSim gates on the even and odd bonds along the ring, as defined in Eq. (2). Additionally, the mirror axis for inversion needs to be centered on a site, not on a bond between two sites. If $\hat{R}$ is the inversion-symmetry operator, which reflects the qubits along this axis, we then have $\hat{R}\hat{U}_{\text{odd}}\hat{R} = \hat{U}_{\text{even}}$, $\hat{R}\hat{U}_{\text{even}}\hat{R} = \hat{U}_{\text{odd}}$, and $\hat{R}\hat{U}_{\text{dec}}\hat{R} = \hat{U}_{\text{dec}}$. For simplicity, we define a modified one-cycle unitary operator

$$\hat{U}_F' = \sqrt{\hat{U}_{\text{dec}}} \, \hat{U}_{\text{even}} \hat{U}_{\text{odd}} \sqrt{\hat{U}_{\text{dec}}}. \quad (3)$$

The operators $\hat{U}_F$ and $\hat{U}'_F$ have the same spectrum, since they differ only by a time shift. It is now easy to see that $\hat{U}'_F = \hat{R}\hat{U}'^T_F\hat{R}$. This can be understood as an additional symmetry, which relates the evolution operator and its transpose, resulting in COE level statistics. Our situation is reminiscent of Ref. [48], where the Floquet spectrum was shown to have COE instead of CUE statistics if there is a transformation which connects the two steps of the Floquet unitary.

Another possibility is when the mirror axis is between two adjacent sites, leading to $\hat{R}\hat{U}_{\text{odd}}\hat{R} = \hat{U}_{\text{odd}}$ and $\hat{R}\hat{U}_{\text{even}}\hat{R} = \hat{U}_{\text{even}}$. We then have $\hat{U}'_F = \hat{R}\hat{U}'^T_F\hat{R}$, meaning that $\hat{R}$ is simply another symmetry of $\hat{U}'_F$ which needs to be resolved. The level statistics in the sector where $\hat{R}$ has eigenvalue $+1$ is then CUE. The only deviations from this expectation are found for small numbers of decorations such as two or four adjacent decorations, where the level statistics after resolving the $\hat{R}$ symmetry is somewhere between COE and CUE. However, it seems to increase towards CUE as the density of decorations or the number of photons is increased. There are also special cases, which are inversion symmetric in respect to both types of mirror axes, such as the pattern with decorations on every third site. In those cases, the level statistics stays COE even after resolving the $\hat{R}$ symmetry. In contrast, all nonsymmetric decoration arrangements were found to exhibit CUE level statistics.

III. SPECTRAL PROPERTIES

In this section we analyze the spectrum of our unitary circuit model in Eq. (2). This model does not have a Hamiltonian representation in general, since the mapping to the XXZ model (Appendix A) is only valid in the $dt \to 0$ limit. As a consequence, the system does not have eigenstates in the usual sense. However, we can instead compute the eigenstates of the one-cycle evolution operator $\hat{U}_F$ Eq. (2), which are known as the Floquet modes. The corresponding Floquet quasienergy spectrum is periodic, with periodicity $2\pi/T$, where T is the time length of one cycle. We set the units such that $T = 1$. We will investigate properties of the Floquet modes and quasienergies by studying their level statistics and the density of states, which tell us about the behavior of the system at very late time scales corresponding to the Heisenberg time. We follow these results by studying the spectral form factor, which reveals similar information at the intermediate Thouless time, relevant for transport.

A. Level statistics

In order to determine whether our model Eq. (2) is integrable or chaotic, we study the statistics of its quasienergy levels ϵ_n. In particular, we examine the level statistics ratio, $r = \min(s_n, s_{n+1})/\max(s_n, s_{n+1})$, characterizing the
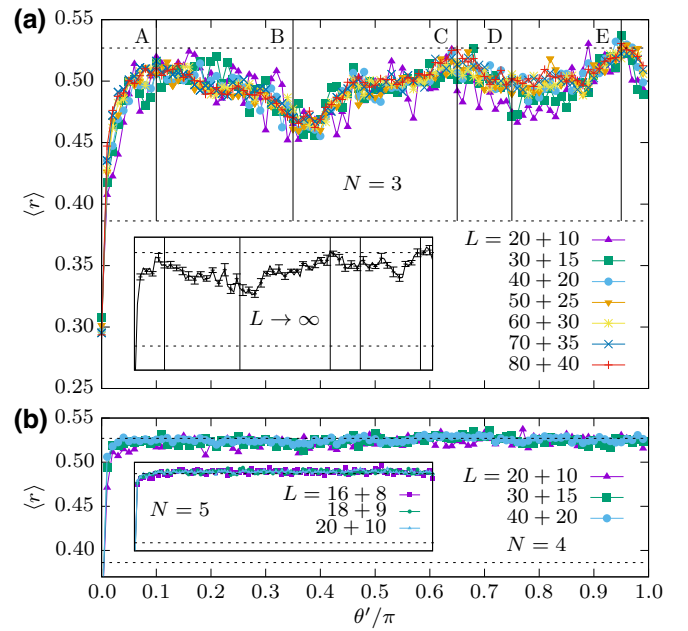

FIG. 2. Statistics of the Floquet quasienergies. Average ratio of consecutive energy gaps $\langle r \rangle$ for different values of θ' with fixed $\theta = \pi/6$, $\phi = 2\pi/3$, $\beta = 0$. The horizontal dashed lines are $\langle r \rangle_{\text{P}} \approx 0.386$ and $\langle r \rangle_{\text{COE}} \approx 0.527$. (a) $N = 3$ photons for different system sizes indicated in the legend. The relevant Hilbert-space dimensions range from $\dim_{L=20+10} = 406$ to $\dim_{L=80+40} = 7021$. The vertical lines A, B, C, D, and E mark several values of θ'/π (0.10, 0.35, 0.65, 0.75, and 0.95, respectively) that will be studied later in more detail. Inset: linear extrapolation to $L \to \infty$. (b) The case of $N = 4$ photons and $N = 5$ photons (inset), with the largest Hilbert-space dimensions $\dim_{L=40+20} = 24405$ and $\dim_{L=20+10} = 14253$, respectively. In all the plots, we resolve the translation symmetry and consider only the $k = 0$ momentum sector.

spacing of adjacent quasienergy gaps $s_n = \epsilon_{n+1} - \epsilon_n$ [49]. When computing $\langle r \rangle$, we omit any exact degeneracies, although such degeneracies are typically absent as long as $\theta' \neq 0$. An integrable system is expected to follow the Poisson distribution with the average value $\langle r \rangle_{\text{P}} \approx 0.386$, while in the chaotic regime the expected distribution for our case, as explained in Sec. II A above, is the circular orthogonal ensemble (COE) with $\langle r \rangle_{\text{COE}} \approx 0.527$ [47,50]. We vary the hopping amplitude θ' between the main chain and the extra sites from 0 to π and plot the corresponding $\langle r \rangle(\theta')$. Figure 2(a) shows the results for $N = 3$ photons for various chain lengths, while the extrapolation to an infinitely large system $L \to \infty$ is plotted in the inset. This result should be contrasted against the results for $N = 4$ and $N = 5$ photons in Fig. 2(b).

Turning on the coupling to the decorations is expected to break integrability, which can indeed be observed in Fig. 2, where the value of $\langle r \rangle(\theta')$ rapidly jumps towards $\langle r \rangle_{\text{COE}}$ as soon as $\theta' \neq 0$. For $N \geq 4$ photons, as soon as $\theta' \gtrsim 0.05\pi$, the level statistics remains pinned to the COE value, in agreement with the usual expectation for

integrability breaking in Hamiltonian systems [51]. However, the case with $N = 3$ photons shows a visible departure from these expectations, exhibiting pronounced dips towards the Poisson value at special values of θ'—see Fig. 2(a). Furthermore, we find that the positions of the dips in $\langle r \rangle$ depend on the main chain hopping amplitude θ, but not on the interaction strength ϕ or the flux through the ring β, see Appendix C. No emergent symmetry, which would explain the dips at certain values of θ', could be identified. Instead, below we will relate the presence of dips with special structures in the density of states of the quasienergy spectrum.

We note that in all cases plotted in Fig. 2, the value of $\langle r \rangle(0)$ lies below the Poisson line, even though the model is known to be integrable at $\theta' = 0$. This is simply due to a large number of degeneracies that arise in the Floquet spectrum due to the disconnected decorations, which produces a strong peak in the probability distribution at zero level spacing. Namely, even though there is no hopping to the extra sites when $\theta' = 0$, there are still states where one or more photons are frozen in these additional sites. A state with all photons outside the main chain has zero energy, as do some states with two separate photons on the main chain and all other photons outside. We found that completely removing the extra sites brings $\langle r \rangle(0)$ closer to $\langle r \rangle_P$, as expected. We also note that, while the hopping amplitudes inside the main chain and between the chain and the extra sites are different, $\theta \neq \theta'$, the nearest-neighbor interaction strength is equal in both cases $\phi = \phi'$. This means that the photons frozen in the decorations can still interact with other photons.

The intriguing features in the level statistics observed in Fig. 2(a) can be understood from the density of states (DOS). The intuition is that sharp peaks in DOS signal a large number of degeneracies in the spectrum, which can decrease the value of $\langle r \rangle$. In Fig. 3(a), we plot the normalized DOS curves for $N = 3$ and $N = 5$ photons at several values of θ' that were marked by A–E in Fig. 2(a). Both photon numbers exhibit a peak at $\epsilon = 0$ when $\theta' = 0$, which is explained by the previously discussed large number of zero modes due to the extra sites. This zero-energy peak is much more prominent for $N = 3$ and its relative height decreases with N. The results for $N = 4$ (not shown) are in between those for $N = 3$ and $N = 5$, with more peaks than $N = 5$, but still overall flatter than $N = 3$. As θ' is increased, the DOS curves become more flat. However, several other notable peaks are present for $N = 3$. Although these peaks are visible at all θ', they are particularly sharp at those values where $\langle r \rangle$ deviates from $\langle r \rangle_{\mathrm{COE}}$ (e.g., $\theta' \in [0.25\pi, 0.45\pi]$ and $\theta' \in [0.75\pi, 0.85\pi]$), see Figs. 2(a) and 3(a), signaling high nonuniformity in the quasienergy spectrum. The peaks in DOS are not present for the nonsymmetric patterns of extra sites, such as a single or three decorations, which will be discussed in Sec. V B.
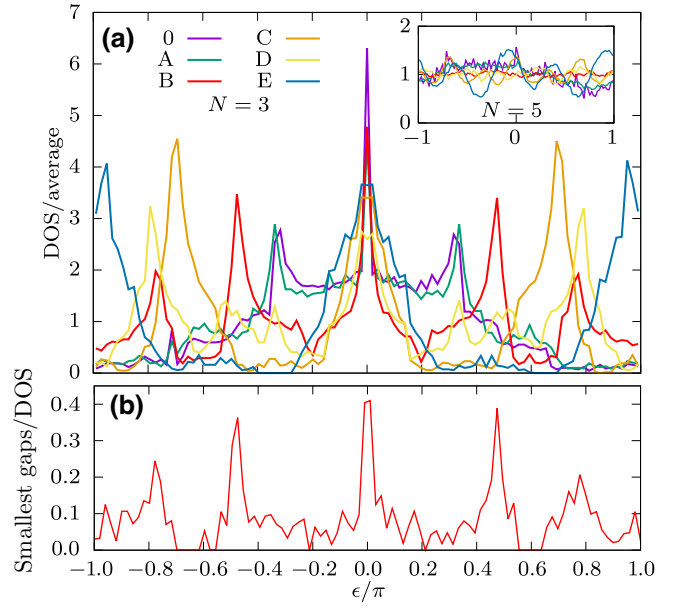

FIG. 3. (a) Density of states (DOS) for different values of θ', normalized by the average over the entire quasienergy spectrum [the labels A–E are defined in Fig. 2(a), while 0 denotes the integrable case $\theta' = 0$]. The main panel corresponds to $N = 3$ photons in a system size $L = 80 + 40$, while the inset shows $N = 5$ in $L = 20 + 10$. In both cases, $\theta = \pi/6$, $\phi = 2\pi/3$. (b) Distribution of the 1000 smallest quasienergy gaps (i.e., about 15% of all levels) throughout the Floquet spectrum, normalized by the local DOS. Data is for $N = 3$ photons in system size $L = 80 + 40$ at $\theta = \pi/6$, $\phi = 2\pi/3$, $\theta' = 0.35\pi$, i.e., for the point labeled B in (a).

At $\theta' = 0$, the peaks in DOS correspond to exact and near degeneracies in the spectrum. Since DOS is probing aggregated features of the spectrum, at finite θ' the peaks do not necessarily demonstrate the presence of near degeneracies between neighboring energy levels that are required for $\langle r \rangle$ to anomalously reduce. However, we find that the smallest gaps between quasienergies are indeed disproportionately concentrated in the towers. In Fig. 3(b), we see that the 1000 smallest quasienergy gaps (normalized by the local DOS) at point B align closely with the location of the towers. Further discussion of the origin of peaks in DOS based on the quasiparticle dispersion relation can be found in Appendix B.

B. Spectral form factor

The level statistics quantities considered above derive from the properties of eigenvalues of the Floquet unitary, hence they describe the behavior of the system at late times. In order to gain information about intermediate times, we study the spectral form factor (SFF) [52]:

$$K(t) = \sum_{m,n} e^{it(\epsilon_n - \epsilon_m)}, \qquad (4)$$

which is defined in terms of two-point correlations between the Floquet quasienergies, ϵ_n. As we set the time period of one unitary cycle to $T = 1$, the time in the above equation is equal to the number of cycles, $t = n_c$.

SFF is known to exhibit starkly different behavior in integrable and chaotic systems, see Refs. [53–56] for some recent examples. In both cases, the SFF at short times is governed by microscopic details of the system and therefore it is nonuniversal. After this initial transient, in integrable systems (Poisson ensemble) the SFF stays approximately constant $K_{\mathrm{P}}(t) \approx \mathcal{H}$, around the value equal to the Hilbert space dimension $\mathcal{H}$. In nonintegrable systems, SFF first reaches a global minimum and, around the Thouless time t_{Th}, it starts to grow approximately linearly, according to the predictions of random matrix theory, until it saturates by the Heisenberg time $t_{\mathrm{H}} \sim \mathcal{H}$. The level statistics and the DOS studied above naturally pertain to the times of order t_{H}, where the discreteness of the Floquet quasienergy spectrum is resolved.

SFF is typically noisy and suffers from a lack of self-averaging [57,58]. In order to smoothen its time dependence, we chose to average it over the flux through the ring β. This parameter does not qualitatively affect the level statistics, as confirmed in Appendix C. Additionally, after averaging over 100 values of $\beta \in [0, \pi]$, we also compute the moving average at each time point by taking into account the nearest 60 points, which finally results in relatively smooth curves. The averaged SFFs for $N = 3$ photons, $L = 60 + 30$ sites and different values of θ' are shown in the inset of Fig. 4(a). After an initial period

of nonuniversal behavior, the SFF for $\theta' = 0$ assumes an approximately constant value, confirming that the system is integrable. In contrast, a clear linear ramp followed by saturation emerges for all studied values of $\theta' > 0$, consistent with broken integrability. We note that the SFF for $\theta' = 0$ saturates at a higher value than $\theta' > 0$, where the plateau is exactly as expected at $\mathcal{H}$. The reason for this is a large number n_0 of zero modes in the integrable case, which increases the late-time value of the SFF to $\mathcal{H} + n_0^2$ (at $\theta' = 0$).

Furthermore, the Thouless time t_{Th} can be extracted from the SFF data. This time gives us the onset of the linear ramp, i.e., the universal behavior described by the random matrix theory. The COE prediction for SFF in the time window $0 < t < \mathcal{H}$ is [47]

$$K_{\mathrm{COE}}(t) = 2t - t \ln(1 + 2t/\mathcal{H}), \tag{5}$$

as shown by the dashed black curve in Fig. 4. In principle, the Thouless time could be defined as the smallest time for which $K(t) = K_{\mathrm{COE}}(t)$. However, since $K(t)$ is typically not smooth enough even after averaging, in practice we use the following criterion to determine the Thouless time [59]:

$$\ln(K(t_{\mathrm{Th}})/K_{\mathrm{COE}}(t_{\mathrm{Th}})) = 0.4. \tag{6}$$

The precise value of the filtering parameter 0.4 is unimportant, as long as it is finite but not too small. In Fig. 4, we plot the extracted Thouless time together with the
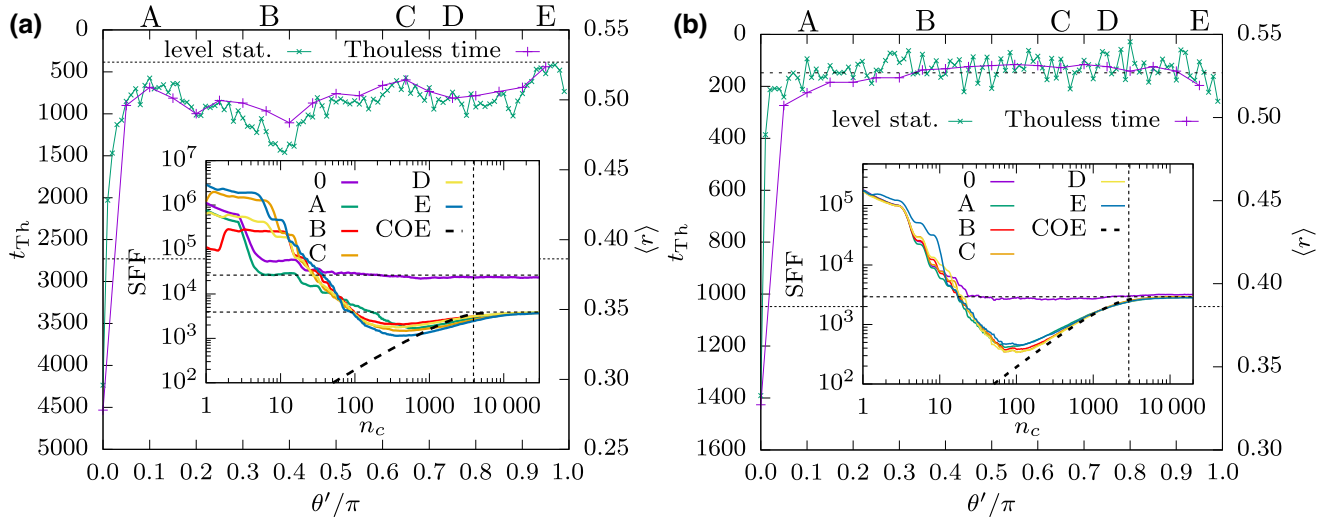

FIG. 4. (a) Comparison of the level statistics ratio $\langle r \rangle$ and the Thouless time extracted from the spectral form factor (SFF) for $N = 3$ photons, $L = 60 + 30$. The labels A, B, C, D, and E mark the special values of θ' from Fig. 2. Inset: SFF time series for several values of θ' indicated in the main panel. The data was averaged over β and smoothened by a moving average (see text). Note the logarithmic scale on both the x and y axis. The horizontal dashed lines mark the saturation values, $\mathcal{H}$ and $\mathcal{H} + n_0^2$, while the vertical line at $n_c = \mathcal{H}$ is the Heisenberg time. The dashed black curve is the COE prediction for the linear ramp. The agreement with COE becomes better as N increases. (b) Same as panel (a) but for $N = 5$ and $L = 14 + 7$, which shows a much clearer linear ramp in the SFF and better agreement with the random matrix theory at late times.

average level-spacing ratio $\langle r \rangle$ for $N = 3$ and varying θ'. Interestingly, the two curves exhibit very similar features, which means that the previously observed deviations in the level statistics for $N = 3$ leave an imprint on the transport properties. The latter—as defined by the Thouless time—occurs later in systems that are farther away from the nonintegrable case, as defined by $\langle r \rangle$.

The agreement of SFF with the random matrix-theory prediction K_{COE} is not particularly good for $N = 3$ photons. This supports our previous observation that the energy spectra in small photon-number sectors have special properties, e.g., as seen in fluctuations of the level statistics and the nonmonotonic DOS. The agreement with COE becomes better as the number of photons N increases, as can be seen for $N = 5$ in Fig. 4(b). The number of zero modes at $\theta' = 0$ is now much smaller than the Hilbert-space dimension, so the dashed horizontal lines at $\mathcal{H}$ and $\mathcal{H} + n_0^2$ are visually indistinguishable. There is also less variance in $K(t)$ curves for different values of $\theta' > 0$, which is reflected in the almost constant value of the extracted Thouless time, as shown in the same figure. This is in line with the level-spacing ratio $\langle r \rangle$, which shows no oscillation with θ' for this photon number but instead remains approximately constant around $\langle r \rangle_{\mathrm{COE}}$.

C. Summary

In this section, we have studied the spectral properties of the Floquet unitary in Eq. (2). We confirmed that integrability is generally broken by $\theta' \neq 0$ in large system sizes. However, at special values of θ', for $N = 3$ photons we also observed a pronounced tendency towards restoration of the Poisson level statistics, see Fig. 2(a). We have related these features in the level statistics to the peaks in the DOS in Fig. 3(a), resulting from an interplay between the geometry of the decorations and the small photon clusters forming the bound states. As these properties derive from the quasienergy spectrum of the Floquet operator, they implicitly relate to the behavior of the system at the very late Heisenberg time. Nevertheless, the study of the SFF showed that similar signatures at these special values of θ' can also be observed at the intermediate Thouless time. A natural question, addressed next, is how these features relate to the dynamics from the special subset of initial conditions associated with bound states of photons.

IV. DYNAMICS OF BOUND STATES

Thus far, we have focused on generic aspects of thermalization at the level of the entire Floquet spectrum of the decorated XXZ circuit in Eq. (2). However, one of the motivations behind the experiment [44] to study this particular model is the fact that its integrable version hosts a special class of ballistically propagating bound states. While such bound states are here protected by integrability, they represent only a fraction of all eigenstates and

therefore it is not hard to imagine that they may persist, due to some other protective mechanism, after integrability is broken. We now examine in detail the stability of such states after decorating the circuit to break its integrability.

In the Ising limit of the Hamiltonian version of the XXZ model, $J_z \gg J$, an N-particle bound state corresponds to N adjacent spins being flipped [25],

$$|000..\underbrace{1\cdots1}_{N}..000\rangle. \tag{7}$$

Even far from the Ising limit when $J_z \geq J$, the behavior of an N-particle bound state can be understood by starting from such an initial state, which is no longer an eigenstate. The same is true for the Floquet XXZ circuit, with the Hamiltonian Ising limit corresponding to $\phi \gg \theta$.

Starting from the initial state (7), the "bound-state probability" (BSP) after n_c cycles is given by

$$\mathcal{B} = \frac{n_T}{n_T + n_S}, \tag{8}$$

where $n_T = \langle \psi(n_c)| \sum_j \prod_{i=j}^{j+(N-1)} \hat{n}_i |\psi(n_c)\rangle$ is the probability of finding photons in N adjacent sites, where the indices i and j label the sites on the main chain. Conversely, the probability of any other N-photon configuration was denoted n_S.

The BSP was experimentally measured in Ref. [44] and found to gradually decay over time even at $\theta' = 0$. This decay was due to experimental imperfections rather than an intrinsic property of the model. For an ideal implementation of the XXZ circuit, the BSP drops rapidly before fluctuating around a steady finite value, as will be shown below. However, once integrability breaking terms are introduced into the circuit, there is no requirement for the N-photon bound states to continue to be stable at late times. Below, we focus on understanding the effect of integrability breaking on BSP dynamics using TEBD simulations implemented in iTensor [46].

The BSP dynamics for $N = 3$, 4, and 5 photon bound states is presented in Figs. 5(a)–5(c) for various strengths of the integrability breaking θ'. By increasing θ' from 0 to $\pi/2$, the decorations become more strongly coupled to the main chain and the bound states are eventually destroyed. However, at intermediate θ' the BSP does not decay to zero, even after many cycles. This is true even when θ' is comparable in size to the natural energy scale along the chain, $\theta' \approx \theta$. For larger bound states, θ' introduces large, slow oscillations into the BSP that are independent of system size. The origin of these oscillations will be explained in Appendix F.

Typically, an infinitesimally small perturbation is sufficient to destroy integrability in the thermodynamic limit $L \to \infty$ and infinite time limit $t \to \infty$. We access these limits by extrapolating the numerical data for the BSP via
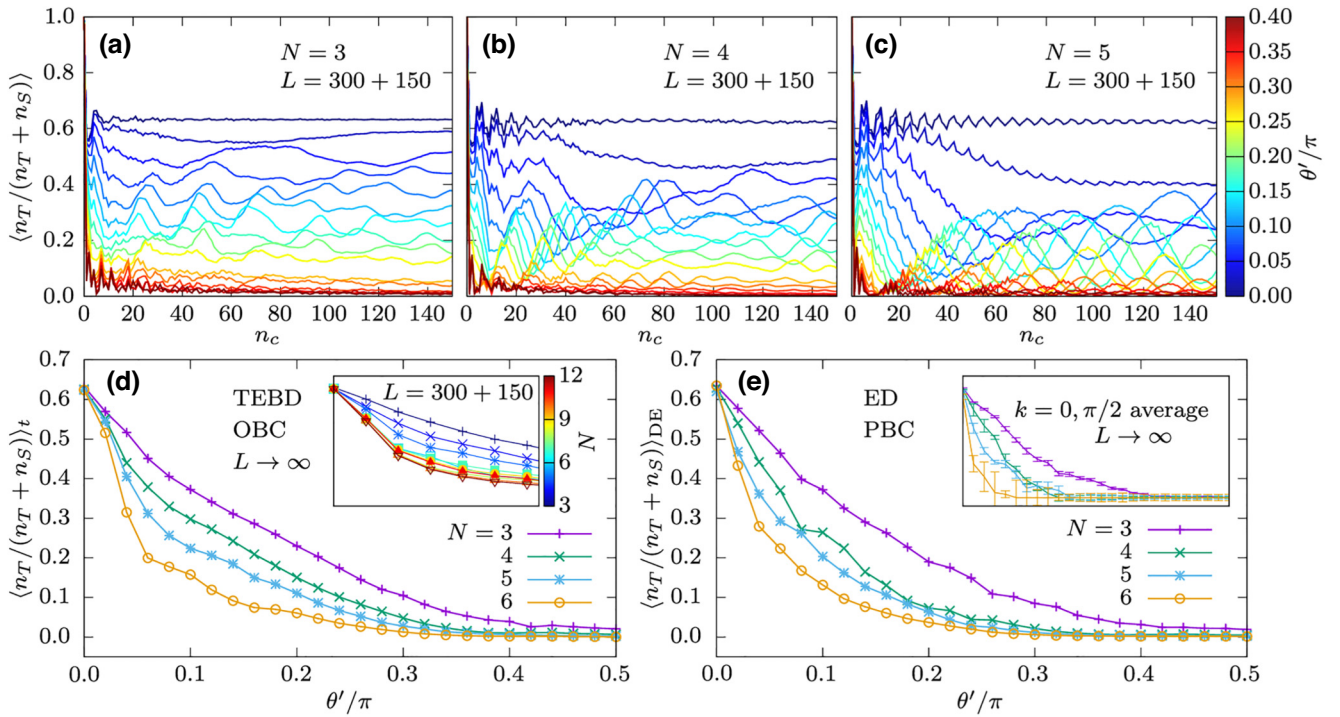
FIG. 5.   (a)–(c) Dynamics of the bound-state probability (BSP) with $\theta = \pi/6$, $\phi = 2\pi/3$, for $N = 3$ photons (a), $N = 4$ (b), and $N = 5$ (c), at fixed system size $L = 300 + 150$. Data is obtained using TEBD with bond dimension $\chi = 256$ and open boundary conditions. (d) Time average of the BSP over 100 cycles using TEBD and extrapolated to $L \to \infty$. We also averaged over two inequivalent initial states (7). The extrapolation errors are smaller than the size of the symbols in the plot. Inset: average BSP for different photon numbers N at fixed $L = 300 + 150$. Data was averaged over 150 cycles and obtained using TEBD with bond dimension $\chi = 320$ for $3 \le N \le 12$, $\theta = \pi/6$, $\phi = 2\pi/3$ and varying θ'. (e) Diagonal ensemble prediction for the probability to remain in a bound state, averaged over two possible initial configurations. Data in this panel is obtained using ED with PBCs, on system sizes $N = 3$, $L = 30 + 15$ (with Hilbert-space dimension dim = 14189); $N = 4$, $L = 20 + 10$ (dim = 27404); $N = 5$, $L = 14 + 7$ (dim = 20348); $N = 6$, $L = 12 + 6$ (dim = 18563). Inset: extrapolation to infinite system size for translation invariant initial configurations, averaged over states with $k = 0$ and $k = \pi/2$ momenta.

two methods: time averaging the TEBD results and evaluating the diagonal ensemble predictions from ED data. The latter directly takes the $t \to \infty$ limit by assuming that the off-diagonal elements of the density matrix average out to zero [15,50]. These two methods have different advantages and limitations. While the TEBD method allows us to study dynamics in very large systems, these simulations become computationally more expensive as the evolution time increases, which limits the total number of cycles. On the other hand, the diagonal ensemble prediction provides information about the BSP at infinite time. This avoids the problems associated with long time scales for decay, which have been observed in quenches involving low density of quasiparticle excitations [60]. However, the diagonal ensemble requires a computation of the complete eigenspectrum using ED, which limits the maximal system size. The total Hilbert-space size is constrained by the amount of RAM available for diagonalization, while our implementation relies on 128-bit integers to represent basis configurations, which limits the maximal number of sites $L \le 128$, irrespective of the photon number N.

In principle, the latter restriction can be lifted using a more flexible encoding of the basis states, at the cost of sacrificing some of the computation efficiency.

For the TEBD time average of the BSP, we consider 100 cycles between cycle $n_c = 20$ and cycle $n_c = 120$ for a variety of system sizes ranging from $L = 20 + 10$ to $L = 300 + 150$. In this way, we exclude the data at very short times, which may be impacted by nonuniversal effects. By fitting the average BSP at each system size according to $\mathrm{BSP}(L, \theta') = \alpha(1/L) + \mathrm{BSP}_\infty$ we extrapolate to $L \to \infty$ and obtain the result plotted in Fig. 5(d). This procedure was repeated for several photon numbers N. In each case, the initial state was chosen according to Eq. (7), which is not translation invariant. As discussed in Sec. II, there are two such inequivalent configurations and our results are averaged over both. We find that the bound states are robust for a finite range of θ', which decreases as the size of the bound states increases.

We also address how the robustness changes as the bound states increase in size, but continue to be dilute relative to the total system size, $N/L \ll 1$. We calculate the

BSP for bound states between sizes $N = 3$ and $N = 12$, averaged over $n_c = 150$ cycles, to find BSP(N, θ'). The results for a fixed number of sites $L = 300 + 150$ are plotted in the inset of Fig. 5(d), where it can be seen that the BSP(N, θ') curves are starting to converge for larger values of N. These results suggest that large but dilute bound states continue to be robust.

The diagonal ensemble results, which directly access the infinite time limit $t \rightarrow \infty$ of the BSP, can be seen in Fig. 5(e). These results are consistent with the extrapolated TEBD results, suggesting small bound states are robust for a finite range of θ'. In particular, the $N = 3$ bound states appear to be robust up to values of the integrability breaking that are comparable to the on-chain hopping terms. As N becomes larger the bound states appear to become less robust, however, both Figs. 5(e) and 5(d) suggest the $N = 4$, $N = 5$, and $N = 6$ bound states are robust for a finite range of θ'.

For our diagonal ensemble calculations in Fig. 5(e) we also averaged over two inequivalent initial configurations (7). Since these states break translation invariance, we have to work in the full Hilbert space and therefore cannot obtain enough data points for reliable system-size scaling. However, if we form a translation-invariant initial state, we can restrict to a particular momentum sector and reach much larger system sizes. This allows us to extrapolate the diagonal ensemble value for BSP to $L \rightarrow \infty$, as shown in the inset of Fig. 5(e), where we have averaged over the $k = 0$ and $k = \pi/2$ sectors. We chose these two values of momenta because we found that they capture the extremal behavior of BSP at small θ': the latter is particularly robust for $k = 0$ and decays most rapidly for $k = \pi/2$, hence their average qualitatively captures the behavior of BSP obtained by averaging over all momentum sectors in the main panel of Fig. 5(e). We emphasize that the observed sensitivity to the momentum sector at $N = 3$ is found to rapidly diminish in larger photon sectors.

In summary, we have shown that the regular decoration pattern, chosen in Ref. [44], gives rise to robust signatures of bound states beyond the integrable regime of the XXZ circuit for photon numbers $N \leq 5$. At long but finite times, these signatures are well converged in system size, as confirmed by TEBD simulations. Moreover, similar conclusions are obtained by considering finite-size scaling of the diagonal ensemble results, pertaining to infinite time, that can be accessed in ED simulations. In Appendix E we show that other observables can reveal a signature of bound states by probing the memory of the initial configuration in Eq. (7) as the system evolves in time. Furthermore, the dynamics of BSP studied above is also reflected in the properties of Floquet eigenstates, in particular their localization in the Fock space and their overlap on the initial state in Eq. (7), which is discussed in Appendix F.

V. FINITE DENSITY OF EXCITATIONS AND OTHER DECORATION PATTERNS

Up to this point, we have mostly focused on the experimental setup of Ref. [44], restricting to the case with integrability-breaking decorations on every other site and small numbers of photons $N \leq 6$. In this section, we consider other cases that were not studied previously. In particular, we will now fix the filling factor instead of fixing the total photon number, which will allow us to investigate convergence to the thermodynamic limit by growing both the system size and the number of excitations, as conventionally done in the literature. Moreover, we will explore other decoration patterns, including those with decorations on every nth site where the system still retains translational invariance, as well as completely random patterns, which break all the symmetries.

A. Fixed filling factor

When we extrapolate systems with small but fixed photon numbers to the infinite number of sites, they become infinitely dilute. By contrast, the thermodynamic limit is conventionally taken by keeping the *density* constant. Thus, we introduce the filling factor $\nu = N/L_{\mathrm{sites}}$ and study properties of our circuit as both N and L_{sites} are simultaneously increased such that ν remains constant.

As done previously for fixed N, we average the BSP (8) over a certain number of cycles and investigate its dependence on θ'. In particular, the averaging was done between cycles $n_c = 100$ to $n_c = 200$, after the initial drop in bound state survival. The time-averaged value is then extrapolated to the thermodynamic limit, while keeping ν fixed, using a quadratic fit in $1/L$, see Fig. 6. Here we set the filling factor to $\nu = 1/10$, but the results for other ν values
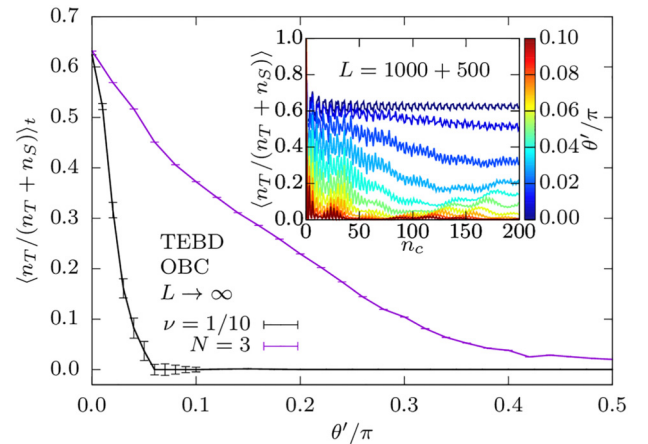

FIG. 6. Time-averaged BSP extrapolated to infinite system size. Filling factor is fixed to $\nu = N/L_{\mathrm{sites}} = 1/10$. For comparison, we also replotted the case of fixed $N = 3$ from Fig. 5. Inset: BSP dynamics for $L = 1000 + 500$ and $N = 100$. All data is obtained by TEBD with bond dimension $\chi = 256$.

are similar. In contrast to dilute systems with fixed photon numbers, the average BSP now drops to very small values already at $\theta' \approx 0.05\pi$. Due to a very slow decay rate of the BSP for very weak integrability breaking $\theta' \lesssim 0.05\pi$, we expect Fig. 6 to provide only an upper bound, as the extrapolated value of the BSP would likely be smaller with an access to a longer time window. However, the TEBD calculations become significantly more time consuming with increasing number of cycles, which is a limiting factor in very large systems.

In the inset of Fig. 6 we show the evolution of BSP for $N = 100$ photons in system size $L = 1000 + 500$, and several values of θ' obtained using TEBD. Unlike the case of fixed but small photon numbers, the large-N bound states are less resilient to integrability breaking by coupling to the extra sites. The BSP quickly decreases with the number of cycles, as can be seen in the inset, where we show only the relatively small coupling strengths $\theta' \in [0, 0.1\pi]$. The extrapolated values in Fig. 6 point to the conclusion that very small photon-number sectors we studied up to this point have unconventional properties, which are not shared by thermodynamically large sectors with nonzero filling factor ν.

B. Other decoration patterns

In this section, we consider the level statistics and BSP dynamics for different patterns of decorations. In Fig. 7 we show the average level-spacing ratio $\langle r \rangle(\theta')$ for $N = 3$ photons and five different types of decoration arrangements. The first one [Fig. 7(a)] is only a single decoration, while the second one [Fig. 7(b)] consists of three decorations attached to sites 2, 4, and 6. Both of these patterns break translation symmetry, which limits the system sizes we can reach. Unlike the level statistics in Fig. 2(a), where $\langle r \rangle$ was oscillatory for $N = 3$, here we observe no such oscillations. Instead, $\langle r \rangle$ first increases to the COE value and then starts to decrease around $\theta' \approx 0.3\pi$. The decrease is not present in larger photon numbers, with the $\langle r \rangle(\theta')$ curve becoming flat already at $N = 4$. Thus, we conclude that $N = 3$ displays anomalous level statistics properties, irrespective of the decoration pattern.

We have also examined the DOS for the patterns of extra sites in Figs. 7(a) and 7(b). The DOS distribution in these cases differs from Fig. 3(a) in that it loses the sharp peaks, but the overall shape stays approximately the same and becomes flatter with increasing number of photons (data not shown). The peaks likely disappear because the new decoration pattern is no longer translation invariant, and the eigenstates, which were previously degenerate are no longer related by symmetry, hence they generally have different energies.

Note that the $\langle r \rangle$ plateau is more pronounced and closer to the COE value for three decorations compared to a single decoration. This trend continues as we add more
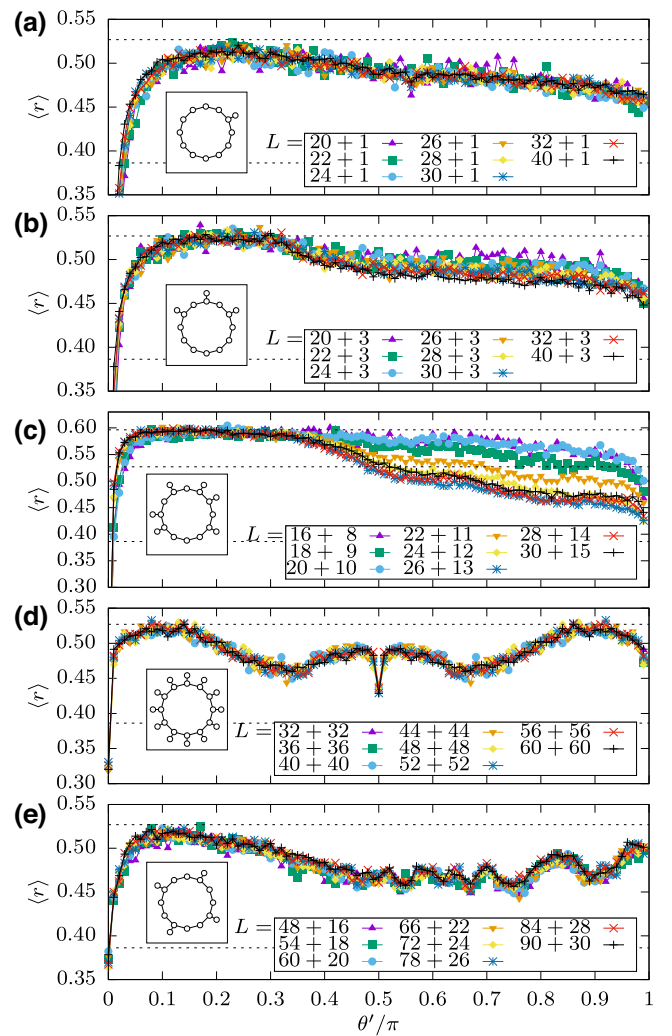

FIG. 7. Level statistics for different decoration patterns (both translation symmetric and nonsymmetric). Data is for $N = 3$ photons, $\theta = \pi/6$, $\phi = 2\pi/3$, and various system sizes specified in legends. The horizontal dashed lines are expectations for the relevant ensembles, $\langle r \rangle_P \approx 0.386$, $\langle r \rangle_{COE} \approx 0.527$, and $\langle r \rangle_{CUE} \approx 0.597$. (a) One decoration on site 2. (b) Three decorations on sites 2, 4, and 6. (c) Random nonsymmetric patterns. (d) Decorations on every site, in the momentum $k = 0$ and inversion-symmetric $I = +1$ sector. (e) Decorations on every third site, $k = 0$, $I = +1$ sector.

decorations. In Fig. 7(c) we show several random patterns where the number of extra sites is equal to half the number of sites inside the ring. We again observe similar behavior, with an initial plateau followed by a decrease in $\langle r \rangle$. However, the plateau is now at the CUE value $\langle r \rangle_{CUE} \approx 0.597$ instead of $\langle r \rangle_{COE} \approx 0.527$. As explained in Sec. II A, this is due to all of the studied random patterns breaking inversion symmetry, unlike the previous cases of one and three decorations. It might seem surprising that $\langle r \rangle$ is nonmonotonic with system size in Fig. 7(c), but this is simply due to choosing completely different patterns for each system size and could be avoided by averaging over several random

patterns for each L. The DOS distribution for the cases in Fig. 7(c) again has no peaks for $\theta' \neq 0$ and is noticeably flatter than the previously considered patterns.

We have also considered two examples of periodic patterns, one with decorations attached to every site of the main ring [Fig. 7(d)] and the other with decorations on every third site [Fig. 7(e)]. The first case is invariant to translations by two sites and inversion, which swaps the ith site (decoration) with $(L_{sites} - i)$th [$(L_{decor} - i)$th], so these symmetries must be resolved in order to obtain the correct level statistics. We note that the full system is not inversion symmetric for the usual periodic pattern with decorations on every other site, even though the arrangement of decorations itself is. This is due to first applying the fSim gates on odd bonds and then on even bonds, Eq. (2). There is no reflection axis, which simultaneously preserves both the decoration pattern and the order of even and odd fSim gate layers. Similar to previous results in Fig. 2(a), for $N = 3$ we again observe deviations from $\langle r \rangle_{COE}$ at certain values of θ'. However, the $\langle r \rangle(\theta')$ curve is now symmetric around $\theta' = \pi/2$ with an integrable point in the middle. This is similar to the case in Fig. 12(a) in Appendix C, where $\langle r \rangle(\theta')$ is symmetric around $\theta = \pi/2$. As can be seen from Eq. (1), this value of the hopping amplitude corresponds to a photon moving to the neighboring site with probability 1, so it is not surprising that this is a special case.

For the second periodic pattern [Fig. 7(e)], the symmetries of the full system are translation by six sites and inversion, which preserves this arrangement of decorations. In this case, we also observe oscillations in $\langle r \rangle(\theta')$, but the local minima and maxima are at different values of θ' compared to the other patterns. As before, all oscillations disappear for $N = 4$ or more photons. For all studied periodic patterns with decorations on every nth site, the DOS still exhibits pronounced peaks for $N = 3$ and to some extent for $N = 4$.

In summary, none of the considered patterns that break translation invariance exhibit oscillations in $\langle r \rangle(\theta')$ that were visible in Fig. 2(a). Instead, $\langle r \rangle$ first reaches a plateau and then starts to slowly decay at larger values of θ'. The plateau is at $\langle r \rangle_{COE}$ for inversion-symmetric patterns and at $\langle r \rangle_{CUE}$ for nonsymmetric ones. For the patterns, which preserve some form of translation symmetry, the level statistics shows similar properties to the experimental case of decorations on every other site, with deviations from $\langle r \rangle_{COE}$ for $N = 3$, albeit with minima and maxima in $\langle r \rangle$ at different locations. Any observed anomalies disappear in larger numbers of photons $N \geq 4$.

Finally, we have also investigated the robustness of bound states for various decoration patterns. In Fig. 8 we plot the averaged BSP for $N = 3$ photons, $L_{sites} = 300$ sites on the main chain averaged over $n_c = 100$ cycles between cycles $n_c = 50$ and $n_c = 150$. For a decoration on every second site we average over the two possible $N = 3$ photon initial states around the center of the chain.
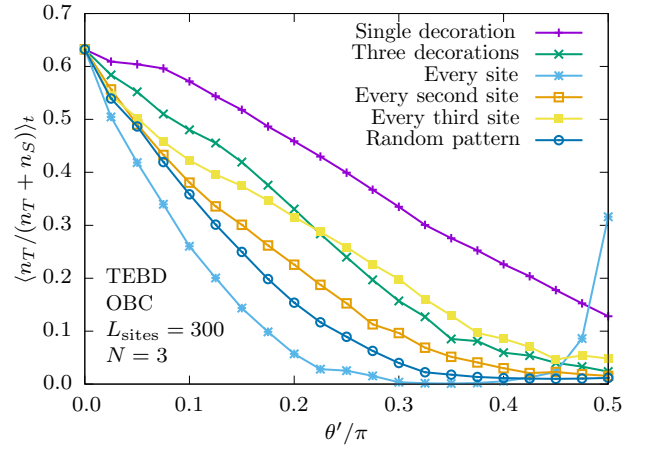

FIG. 8. Time-averaged BSP over 100 cycles for different decoration patterns in the $N = 3$ excitation sector for $L_{sites} = 300$. The fixed parameters are $\theta = \pi/6$, $\phi = 2\pi/3$, and $\chi = 256$. In the case of decorations on every second (third) site the results were averaged over two (three) nonequivalent initial bound-state configurations. The random pattern results were averaged over five different patterns with decorations on half of the sites, $L_{decor}/L_{sites} = 1/2$.

We perform a similar averaging over the three possible initial states for the case of a decoration on every third site. For randomly allocated decorations we instead average over five different random patterns with the initial bound state at the center of the chain. These results suggest the robustness of the bound states is more dependent on the density of decorations L_{decor}/L_{sites} than on the actual pattern. The bound states survive for larger values of θ' when the number of decorations is smaller. The average BSP decays over a similar range of θ' for random patterns with $L_{decor}/L_{sites} = 1/2$ and for the periodic case of the same site density. For the case of decorations on every site there is a peak at $\theta' = \pi/2$, which corresponds to the near integrable point as seen in Fig. 7(d). As before, the bound states become increasingly less robust as the number of photons grows.

VI. CONCLUSIONS AND DISCUSSION

We have performed systematic classical simulations of the Floquet XXZ circuit on a 1D chain with integrability breaking decorations. This study was motivated by the recent Google experiment [44], which realized the same model on a ring of superconducting qubits and investigated the dynamics of its bound states. Surprisingly, the bound states were observed to be resilient to integrability-breaking perturbations in the form of extra qubits attached to the ring. We have analyzed the level statistics of this model and simulated the dynamics of bound states, confirming that some of these states indeed survive in certain parts of the nonintegrable regime, even for an infinite number of qubits and at infinite time. In

contrast to much previous work, the focus of Ref. [44] and our own was on dilute systems containing *few* excitations. Such models have been studied in the context of "weak" quenches [60,61], the onset of quantum chaos in few-body systems [62], and meson bound states [63–69]. As we have demonstrated, the latter are amenable to classical simulations in large numbers of qubits, providing useful benchmarks for future studies on improved quantum hardware.

One of our most significant findings is that small but fixed photon-number sectors show unusual properties in several respects. In particular, the robustness of bound states depends on the photon number, with larger states decaying more rapidly as the coupling to the integrability-breaking extra sites is increased. Moreover, the energy spectrum for $N = 3$ photons has unusual level statistics, which deviates from the expectation for a chaotic system even for strong couplings to the integrability-breaking decorations. As discussed in more detail in Appendices B and D, this can be attributed to the presence of special eigenstates in the energy spectrum. These eigenstates have a relatively simple structure, which is related to one-photon and two-photon states, while the rest of the photons are located in the decorations. The proportion of such states is large enough only in sufficiently dilute systems. When the decoration pattern is periodic, some of these eigenstates are related by translation and are therefore degenerate in energy, which results in prominent peaks in the DOS and affects the level statistics. The deviations in level statistics were shown to leave an imprint in the dynamics of bound states by slowing down the thermalization.

Additionally, we have investigated systems with constant filling factors and their extrapolation to the thermodynamic limit. Such systems are no longer dilute and our findings indicate that they do not support stable bound states when integrability is broken. This is in stark contrast with the bound states in very dilute systems with small photon numbers, such as the one studied in experiment [44]. Moreover, we have explored other decoration patterns, including both periodic and nonperiodic ones. A brief summary of all considered systems is given in Table I. Our calculations suggest that the peaks in the density of states disappear when the pattern is not periodic, which destroys the translation symmetry of the full system. This is likely a consequence of certain eigenstates no longer being degenerate. We also find that the inversion symmetry of the decoration patterns (or lack of it) influences the level statistics. In particular, inversion-symmetric patterns are consistent with COE and nonsymmetric with CUE statistics in the chaotic regime. Deviations from these values were observed only for $N = 3$ photons and were found to diminish as the number of photons is increased. However, our results do not indicate a link between the irregularities in the level statistics and the robustness of bound states, although both properties are most prominent in dilute systems. For example, nonperiodic decoration patterns result in level-spacing ratios consistent with random matrix theory, implying that the integrability is indeed fully broken, while the few-photon bound states remain robust in that regime.

One advantage of the classical simulations performed in this work is direct access to the system's properties at finite energy densities. Thus, the model considered here would

TABLE I.   Brief summary of different systems studied in this work. N is the number of photons, L_{sites} is the number of sites on the main chain, and L_{decor} the number of decorations, while $\nu = N/L_{\text{sites}}$ is the filling factor. Periodic patterns are those with decorations on every single, second, third, fourth, or fifth site.

N	$L_{\text{decor}}/L_{\text{sites}}$	pattern	robust bound states	level statistics	DOS	Figs.
3	1 1/2 1/3 1/4 1/5	periodic	✓	oscillating $\langle r \rangle(\theta)$	sharp peaks	7(d) 2(a), 3 7(e)
3	single decoration three decorations	non-periodic	✓	$\langle r \rangle_{\text{COE}}$ plateau then decrease	no peaks	7(a) 7(b)
3	1/2	random	✓	$\langle r \rangle_{\text{CUE}}$ plateau then decrease	no peaks	7(c)
4 and 5	1 1/2 1/3	periodic	✓	$\langle r \rangle_{\text{COE}}$ for $\theta' \gtrsim 0.05\pi$	relatively flat	2(b), 3(a)
4 and 5	single decoration three decorations	non-periodic	✓	$\langle r \rangle_{\text{COE}}$ for $\theta' \gtrsim 0.05\pi$	relatively flat	not shown
4 and 5	1/2	random	✓	$\langle r \rangle_{\text{CUE}}$ for $\theta' \gtrsim 0.05\pi$	relatively flat	not shown
$\nu = 1/10$	1/2	periodic	✗	not computed	not computed	6

be useful for benchmarking quantum algorithms that target states at a finite energy density [70]. Moreover, it would be interesting to explore other models that host bound states, e.g., the chiral Hubbard model [45], and investigate if such models exhibit similar behavior in relation to the density of excitations and integrability breaking by changing the geometry of the system, as described in this work.

Note added.—Recently, we became aware of Ref. [71], which also studied the stability of bound eigenstates in the special case of $N = 3$ photons and decorations on every second qubit. Based on perturbative arguments and the scaling of inverse participation ratio, Ref. [71] concluded that $N = 3$ eigenstates slowly lose their bound-state character in the $L \to \infty$ limit. Our finite-size scaling analysis above suggests that the bound state probability remains finite in this limit for $N = 3$, however this cannot rule out the possibility of a much larger length scale, at which all dynamical signatures of bound states would ultimately disappear at infinite time.

APPENDIX A: CONTINUOUS MODEL

For simplicity, here we assume a decoration pattern where one extra site is attached to every even site of the main ring with PBCs. The continuous XXZ Hamiltonian, which corresponds to the unitary circuit from Eqs. (1) and (2) in the $dt \to 0$ limit is

$$
\begin{aligned}
H_{\text{XXZ}} &= \sum_{i=1}^{L_{\text{sites}}} J(e^{i\beta} \sigma_+^i \sigma_-^{i+1} + e^{-i\beta} \sigma_-^i \sigma_+^{i+1}) + J_z(\sigma_z^i \sigma_z^{i+1}) \\
&+ \sum_{i=1}^{L_{\text{decor}}} J'(e^{i\beta} \sigma_+^{2i} \sigma_-^{e_i} + e^{-i\beta} \sigma_-^{2i} \sigma_+^{e_i}) + J_z'(\sigma_z^{2i} \sigma_z^{e_i}) \\
&+ \sum_{i=1}^{L_{\text{sites}}} h_z(i) \sigma_z^i + \sum_{i=1}^{L_{\text{decor}}} h_z^e \sigma_z^{e_i}, \qquad (A1)
\end{aligned}
$$

where e_i are the integrability-breaking extra sites attached to even sites $2i$. The local field is $h_z(2i+1) = -2J_z$ on odd sites, $h_z(2i) = -3J_z$ on even sites and $h_z^e = -J_z$ on extra sites. Additionally, if we impose OBCs and an even number of sites, the local field is $h_z(1) = -J_z$ on the first site and $h_z(L) = -2J_z$ on the last site. The corresponding unitary circuit parameters are $\theta = 2Jdt$, $\phi = 2J_zdt$, $\theta' = 2J'dt$, and $\phi' = 2J_z'dt$. This continuous model can be easily generalized to an arbitrary decoration pattern by changing the local fields.

APPENDIX B: ORIGIN OF PEAKS IN THE DENSITY OF STATES

The sharp peaks in DOS can be attributed to the existence of special eigenstates with a relatively simple structure obtained by combining single-photon and two-photon states. Analytical expressions for the dispersions of a single photon or N-bound photons in the integrable (non-decorated) circuit are known [45]. Adding the decorations with $\theta' = 0$ results in an additional zero-energy band in the single-photon dispersion, since all the photons in the extra sites are frozen. This means that, for example, single-photon and two-photon eigenstates are still present in the three-photon spectrum at $\theta' = 0$, since we can just move the remaining photons to the decorations, where they will have zero energy.

In Fig. 9(a), we compare the actual two-photon Floquet spectrum (dots) with the states constructed from two single-photon states (crosses). The color scale represents the deviation from the nearest analytically constructed state. The agreement is remarkably good, which is not surprising given that the system is very dilute and only nearest-neighbor interactions are present. The two bands at the bottom of the plot are two-photon bound states, which are also in agreement with analytical expressions from Ref. [45]. Figure 9(a) is for the integrable case with no extra sites. Adding the decorations leads to the appearance of two additional bands, see Fig. 9(b) and compare with (a). The first one is a bound-state band, which corresponds to one photon in the main chain and another in adjacent decoration and is completely flat. The second one is a wider band of single-photon states corresponding to one photon inside and the other in a nonadjacent decoration. This wider band is centered around zero and has high DOS on its edges, which coincides with the peaks around $\pm\pi/3$ in three-photon DOS from Fig. 3(a). Another smaller peak in DOS around -0.75π comes from the flat band of two bound photons.

We can conclude from the previous discussion that the three-photon DOS is strongly influenced by special single- and two-photon eigenstates. This effect is not so prominent in DOS for four or more photons. This is because the number of special states is much smaller compared to the total
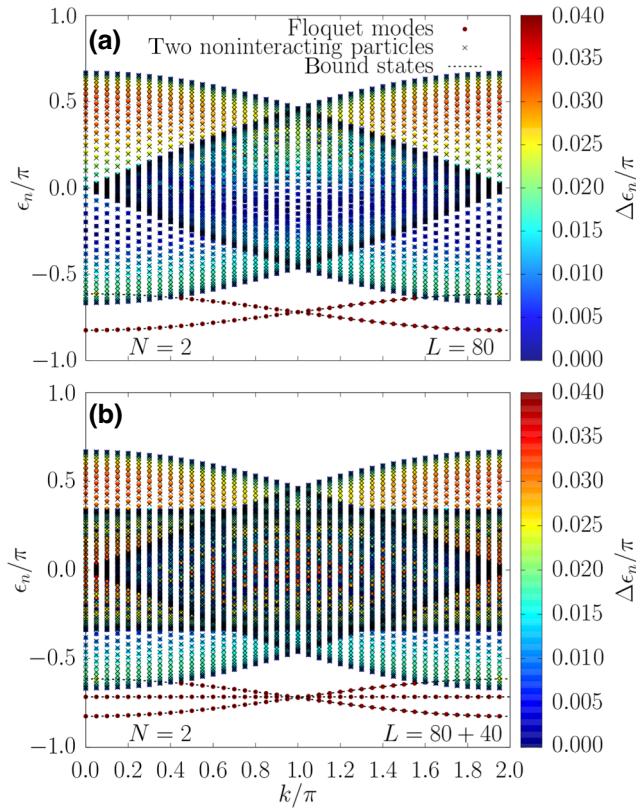
FIG. 9. (a) Comparison of the actual dispersion of two-photon states for the integrable case $\theta' = 0$ with no extra sites (dots) and the theoretical prediction for two separate noninteracting photons (crosses) and two bound photons (dashed lines). The color scale corresponds to the deviation between each dot and the closest cross. (b) Same as (a) but with added extra sites, while $\theta' = 0$.

Hilbert-space size but also due to the special states becoming more uniformly distributed through the quasienergy spectrum. In Appendix D we quantify this and show that the proportion of special states for a fixed photon number N becomes asymptotically independent of the system size L. However, the saturation value still strongly depends on N, e.g., the special states comprise as many as 70% of all states for $N = 3$ but only 1% for $N = 8$.

This previous analysis can now be extended to finite values of θ'. Analytical expressions for the single-photon dispersion are not available in this case, but can be easily numerically computed for different coupling strengths θ'. There are still three different bands, since each unit cell contains three sites. We then construct three-photon bands by taking combinations of the single-particle bands, neglecting the interactions between the particles. This is a good approximation in a dilute system, even with nonzero interaction strength. For three photons we obtain ten different bands, one for each combination of the three bands. We label the combination in which all photons come from the first band 111, two photons in first and one in second 112, one photon in the first, second, and third 123, etc. The
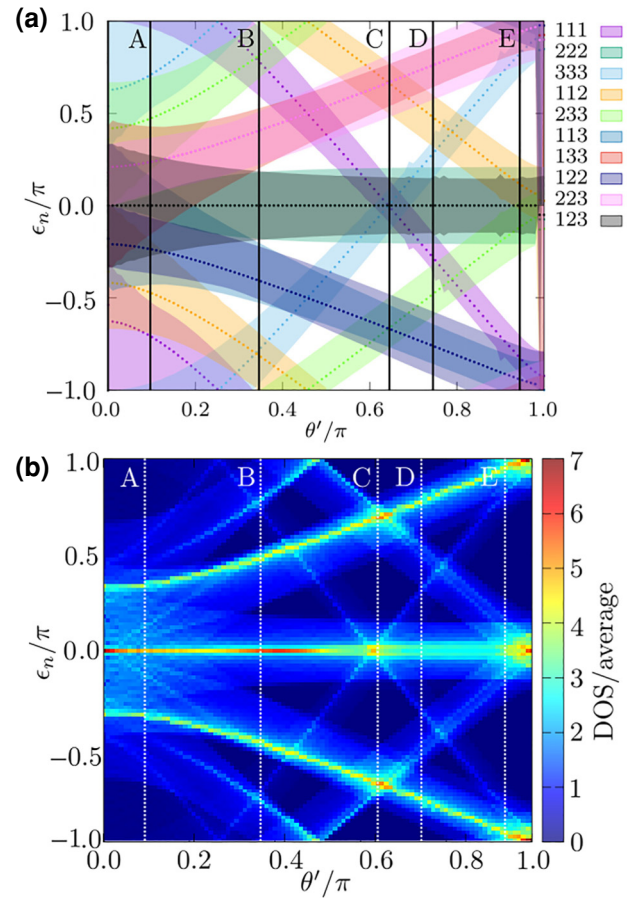

FIG. 10. (a) Bands of special states constructed by taking linear combinations of numerically obtained single-photon bands for $\theta' \in [0, \pi]$. Here we consider the case of $N = 3$ separate photons. The bands are labeled by three numbers, stating if each photon is in the first (1), second (2), and third (3) single-photon band. (b) Corresponding DOS. The bright regions can be related to the peaks in Fig. 3. The vertical lines A, B, C, D, and E mark special values of θ' from Fig. 2.

dependence of these bands of special states on θ' is shown in Fig. 10(a). As θ' is increased, the bands move and cross each other.

The DOS is typically higher near the edges of the bands, so we expect the DOS to be amplified when two bands cross. The edges of 222 and 123 bands overlap around $\theta' = 0.35\pi$, which is where the level-spacing ratio deviates the most from $\langle r \rangle_{\text{COE}}$. Several other bands also overlap around this point. The DOS plot for the special bands shown in Fig. 10(b) roughly corresponds to the peaks in Fig. 3(a). Therefore, as in the $\theta' = 0$ case, the peaks in DOS at $\theta' \neq 0$ are also explained by the special states, which comprise a large proportion of the Hilbert space in systems with smaller numbers of photons, such as $N = 3$. However, it is not obvious from Fig. 10(b) in which θ' regions the level statistics deviates the most from the value expected in

chaotic systems. In particular, there are three very prominent peaks around $\theta' = 0.65\pi$, where the level-spacing distribution is actually very close to COE. We conjecture that these peaks are not narrow enough to lead to a sufficient number of degeneracies that could affect the level statistics. One might expect that the specially constructed states are a better approximation for a noninteracting system and that the $\langle r \rangle(\theta')$ dependence would look different at smaller values of the interaction strength ϕ. This, however, is not the case, as shown in Appendix C, where it can be observed that the level statistics barely changes with ϕ.

APPENDIX C: EFFECT OF PARAMETERS θ, ϕ, AND β

Throughout this paper, we have mostly considered the parameters $\theta = \pi/6$, $\phi = 2\pi/3$, and $\beta = 0$, which were used in the experiment from Ref. [44]. In this Appendix, we explore the effects of changing these parameters. First we perform a scan of the parameter space over a range of interaction strengths ϕ and couplings to the extra sites θ' while keeping the hopping amplitude inside the ring fixed to $\pi/6$. The BSP for an initial state of $N = 3$ bound photons, Eq. (7), averaged over the first $n_c = 50$ unitary cycles, is shown in Fig. 11. Here we also average over two nonequivalent initial configurations, although the plot looks very similar without averaging. The results are symmetric to reflection around the $\phi = \pi$ and $\theta' = \pi$ axes, which is unsurprising as these reflections result only in minus signs in certain matrix elements from Eq. (1) [$\sin(2\pi - \theta') = -\sin(\theta')$ and $e^{i(2\pi - \phi)} = e^{-i\phi}$].

The region of interest is the bottom part of this figure, with intermediate ϕ and small θ'. There is a minimal value of interaction strength required for the survival of

bound states, $\phi_{\min} \approx \pi/3 \approx 2\theta$. This is in line with previous analytical results, which state that the bound states exist for any momentum in the gapped regime $\phi > 2\theta$ [45]. The maximal decoration coupling, which supports the bound states, is around $\theta' = \pi/3$ and does not significantly depend on ϕ. There are also additional regions where the bound states remain stable, such as around $\phi = \pi/3$ and $\theta' = \pi$. However, the $\theta' = \pi$ line is a special case since there is no hopping from the main chain to the extra sites, see Eq. (1). We therefore did not focus on these regions of the phase diagram. We have also investigated the cases of $N = 4$ or more photons in the initial bound state and these plots show similar features to $N = 3$. The main difference is that the region with robust bound states shrinks in the θ' direction with increasing N, which is consistent with our results from Figs. 5(d) and 5(e).

In Fig. 12 we plot the average level-spacing ratio $\langle r \rangle(\theta')$ for several values of the parameters θ, ϕ, and β. As can be observed in Fig. 12(a), the oscillations in $\langle r \rangle(\theta')$ are visible for all values of the hopping amplitude θ, but the exact positions of the local minima and maxima depend on θ. The most distinctive case is $\theta = \pi/2$, where the level statistics is close to Poisson for most values of θ'. According to Eq. (1), this is a special case where the hopping probability on the main chain is 1 in each cycle. Additionally, we note that the $\langle r \rangle(\theta')$ curve is the same for θ and $\pi - \theta$.

FIG. 12. Level statistics for different values of parameter θ (a), ϕ (b), and β (c). The only parameter that significantly affects the results is the hopping amplitude θ. We note that $\theta = \pi/2$ is a special case where the probability of hopping to the neighboring site is 1 in each cycle, see Eq. (1). It is therefore not surprising that this case is close to being integrable.
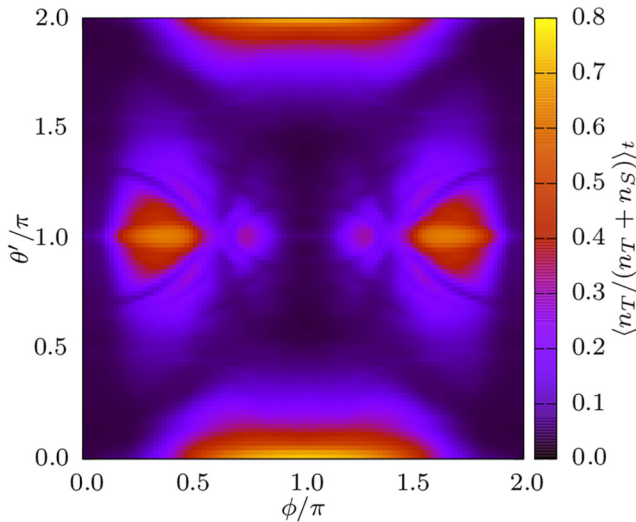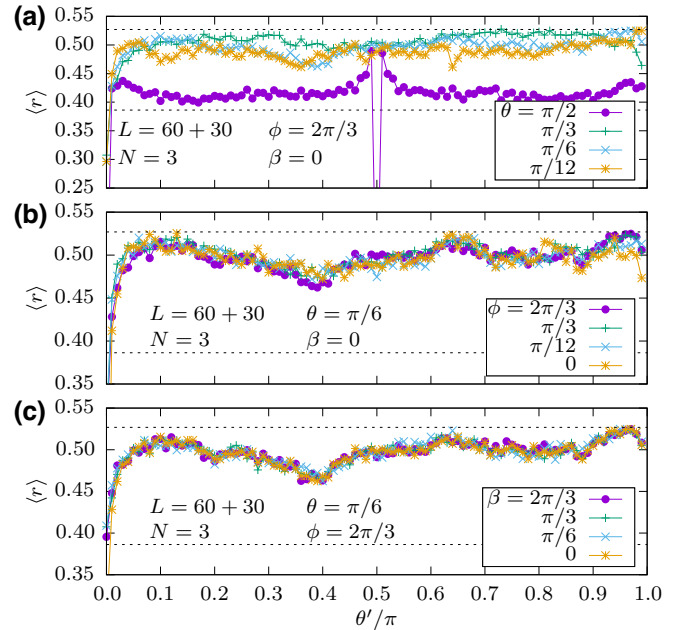
FIG. 11. Bound-state probability averaged over $n_c = 50$ cycles and two different initial configurations. $L = 40 + 20$, $N = 3$, $\theta = \pi/6$, $\beta = 0$, $\theta' \in [0, 2\pi]$, and $\phi \in [0, 2\pi]$.

In contrast to θ, the other two parameters ϕ and β have almost no effect on the level statistics. The dependence on the nearest-neighbor interaction strength ϕ is shown in Fig. 12(b). This further supports the conclusion that the deviations from $\langle r \rangle_{\text{COE}}$ are mainly a consequence of three separate photon states whose energies do not depend on ϕ. The magnetic flux through the ring β has even less influence on the results, see Fig. 12(c). However, it does change the actual energy levels. For this reason, the parameter β was very useful for averaging the spectral form factor in Sec. IV.

APPENDIX D: DENSITY OF EXCITATIONS

We have previously attributed the deviations from the chaotic level statistics and sharp peaks in DOS to the existence of special eigenstates in Sec. B. These features were more pronounced for small photon numbers such as $N = 3$. In Fig. 13 we show the proportion of some simple basis configurations in total Hilbert spaces of systems with different fixed numbers of photons N and increasing number of sites L. In particular, these are the configurations with all photons outside the main chain, just one photon inside, two separate photons inside, and two bound photons inside. The special eigenstates that affect the spectral statistics are superpositions of such configurations. They are highly degenerate in energy, due to diluteness of the system and large number of possible configurations of photons in the extra sites, which results in peaks in DOS and deviations in the average ratio of consecutive energy gaps.

For all photon numbers considered, the proportion saturates at some constant value as the size increases and the system becomes sufficiently dilute. Indeed, the saturation
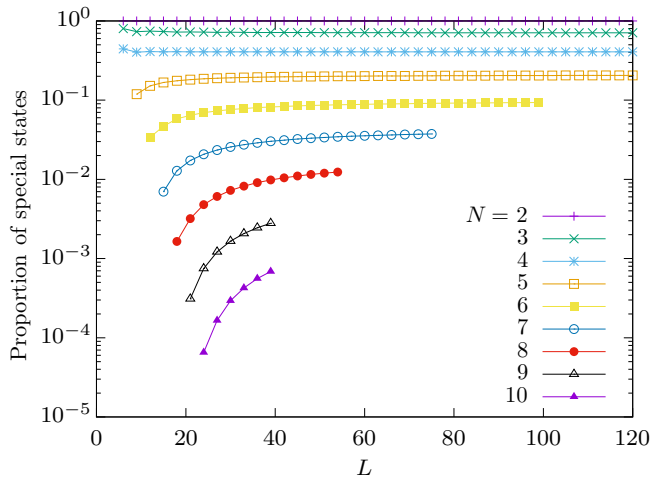
value is much larger for $N = 3$ (approximately 70%) than it is in cases of more photons (e.g., around 1% for $N = 8$). This explains why the special states have much stronger effects on the spectra of systems with small photon numbers. Such states are still present in large-N systems, but their proportion is negligible and thus has practically no influence on the energy spectrum. We note that the proportion of special states depends on the ratio between the number of decorations and the number of sites $L_{\text{decor}}/L_{\text{sites}}$, which is equal to $1/2$ in the case shown here. More decorations would result in a larger proportion of these states.

APPENDIX E: MEMORY OF THE INITIAL STATE

The BSP is not the only local observable that reveals the unusual behavior of the bound initial states at finite θ'. Persistent nonthermalizing behavior can also be seen in the site occupation, $n_i = \langle \hat{n}_i \rangle$. Since the integrability breaking decorations make up one third of the total sites on the chain, we would expect a third of the photons to be located on them after a short time when the system has sufficiently thermalized. Instead, we find that this is only true at larger $\theta' \gtrsim \pi/3$. The fraction of photons located on the decorations as θ' is varied shows very similar behavior for bound states of different sizes.

In the integrable case, larger bound states propagate more slowly due to their small group velocity [44,45]. This behavior appears to persist in the nonintegrable model. A large fraction of photons in the bound state remain in the vicinity of their initial sites even after many cycles. In
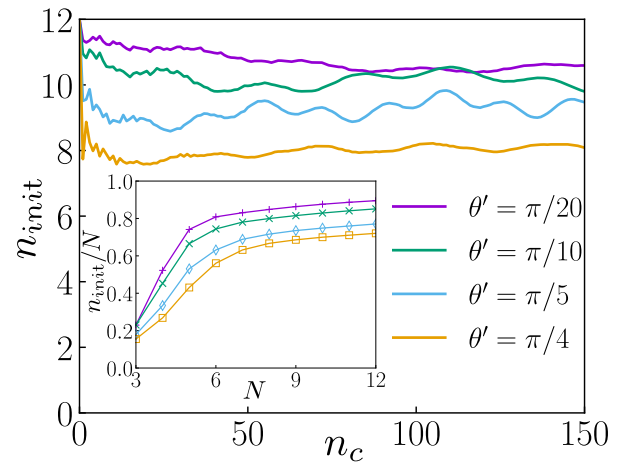

FIG. 13. Proportion of special configurations for different photon numbers N and system sizes $L = L_{\text{sites}} + L_{\text{decor}}$. The decorations are on every other site. These simple states can be constructed by combining single-photon and two-photon configurations with photons in the extra sites.

FIG. 14. Continued occupation of sites initially occupied by an $N = 12$ photon bound state after n_c cycles. Data is obtained by TEBD for a system size $L = 300 + 150$, bond dimension $\chi = 320$ for $\theta = \pi/6$, $\phi = 2\pi/3$ and a few values of θ' indicated in the legend. Inset: n_{init}/N for bound states of sizes $N = 3$ to $N = 12$ at different values of θ'. Data is obtained by TEBD for 150 cycles and the same parameters as in the main plot.

Fig. 14, we show $n_{\text{init}} = \sum_{i \in \text{initial sites}} n_i$ for an $N = 12$ photon bound state for different θ', demonstrating this robust nonthermalizing behavior. The average of n_{init} for different size bound states can be seen in the inset of Fig. 14. From this perspective, the bound states appear to grow more robust as they increase in size. This at first seems to be in contradiction with the BSP results from Fig. 5. However, the BSP measures the overlap with the N-photon bound state as a whole, while n_{init} also captures the case when the bound state loses photons from the edges while its core stays robust and does not move away significantly from its initial position. This is precisely what happens for large-N bound states. Since we are considering hardcore bosons, the photons from the middle of the bound state can only hop to the decorations and back, while the photons at the edge can move further away along the chain and become detached from the rest.

APPENDIX F: PROPERTIES OF FLOQUET MODES

In Sec. IV, we demonstrated the robustness of the bound states in the dynamics. These results are naturally reflected in the anomalous properties of special eigenstates associated with bound states, which we investigate in detail in this Appendix. As a generic measure of eigenstate localization in the Fock space, it is customary to study the inverse participation ratio (IPR). For a (normalized) eigenstate $|\psi_{i,k}\rangle$ of the Floquet unitary $\hat{U}_F$ with momentum k, we define the IPR as

$$\text{IPR}_k = \sum_n |\langle \psi_{i,k} | k_n \rangle|^4, \qquad \text{(F1)}$$

where, for convenience, we take $|k_n\rangle$ to be the momentum basis states. For sufficiently small θ', the eigenstates with largest support on the bound state can be uniquely identified with the aid of the BSP in Eq. (8). In a fixed momentum sector, there are four bound eigenstates corresponding to the largest BSP: two which have all the excitations on the main chain, and two where one of the excitations is on a decoration. A natural question is how localized these eigenstates are in the Fock space, e.g., whether their IPR asymptotically converges to a constant or decays as a power law, $L_{\text{sites}}^{-\alpha}$, in the limit $L_{\text{sites}} \to \infty$.

In Fig. 15 we plot the averaged IPR of the four bound eigenstates for $\theta' = 0.1\pi$ and different system sizes in the $N = 3$ sector. We find the IPR has strong fluctuations between different system sizes, even after averaging over the four bound states in the given momentum sector. Contrasting the linear plot against the log-log plot shown in the inset of Fig. 15, it is difficult to ascertain the asymptotic behavior of IPR, in particular for larger values of θ' such as 0.3π, where power-law decay remains a possibility. For
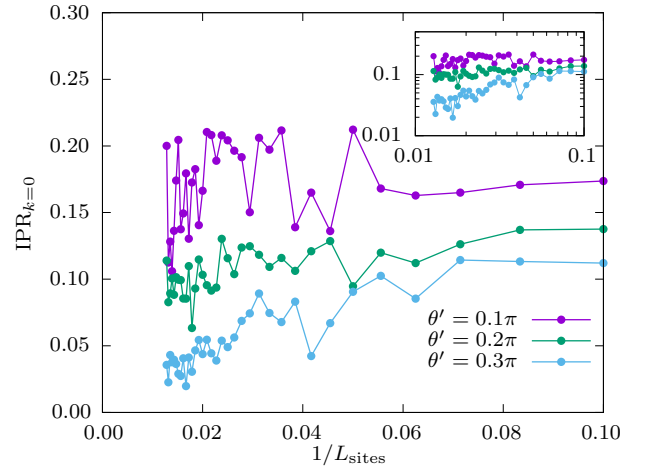

FIG. 15. Finite-size scaling of IPR, Eq. (F1), for three values of θ'. We plot the average IPR for the four bound eigenstates in $k = 0$ momentum sector. Inset shows the same data on a log-log scale.

this reason, in the main text we focused on the dynamical properties, which show smoother convergence while (at finite times) are also readily accessible in experiment.

A finer characterization of the Floquet modes is obtained by plotting their overlap with the bound initial state (7), against the number of pairs of neighboring occupied sites on the main chain, $\langle \psi | \sum_i \hat{n}_i \hat{n}_{i+1} | \psi \rangle$, in each Floquet mode. This is shown in Figs. 16(a) and 16(b), for the case of $N = 3$ photons, contrasting the integrable case with that of $\theta' = 0.2\pi$. For $N = 3$, the number of neighboring occupied sites can be at most 2, corresponding to a three-photon bound state. Alternatively, the value 1 corresponds to two neighboring and one separate photon, while 0 implies three separate photons. The integrable case, $\theta' = 0$, in Fig. 16(a) displays three separate sectors, one of which contains the bound states (red points). The energies of these sectors overlap, but there is no mixing between the states. The overlapping energies are a consequence of the periodic Floquet spectrum, while in the Hamiltonian XXZ model these sectors are separated by energy gaps. As θ' is increased, the system becomes nonintegrable and the sectors start to mix. At $\theta' = 0.2\pi$, Fig. 16(b), the bound states have almost merged with the bulk, but still remain visible. This is no longer the case after $\theta' = 0.3\pi$, which is consistent with the results of Figs. 5(d) and 5(e) where it was shown that the bound states are robust only up to this point.

The overlap plots for larger numbers of photons display similar features to $N = 3$. At $\theta' = 0$, there are N separate sectors, which are defined by the number of pairs of adjacent photons. The bound Floquet modes slowly mix with the other sectors as the coupling to the decorations in increased. The case of $N = 5$ and $\theta' = 0.1\pi$ is shown in Fig. 16(c). Here we see three prominent towers of states, which are related to the oscillations in the BSP in Fig. 5(c).
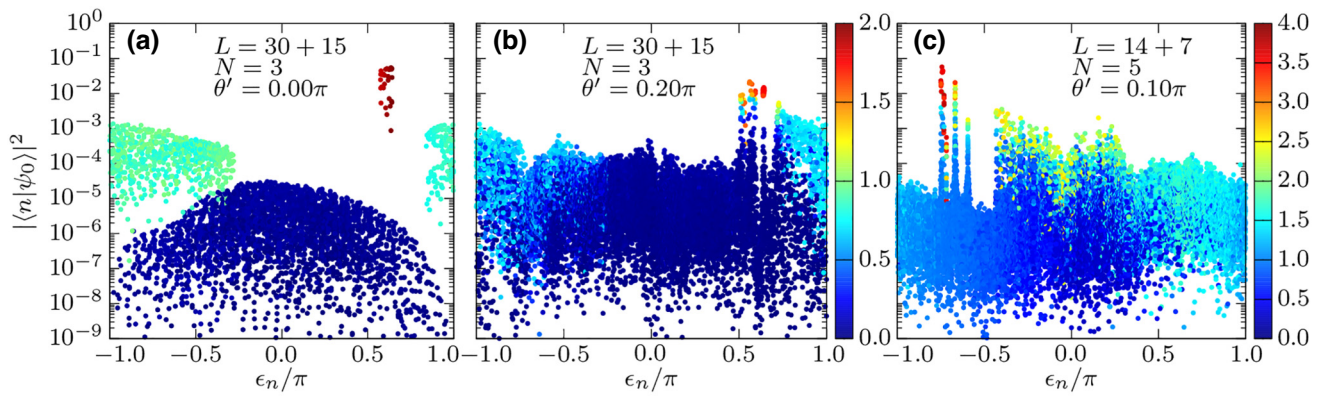
FIG. 16. Overlap of the initial state with the eigenstates of the one-cycle evolution operator. (a),(b) $N = 3$ photons in system size $L = 30 + 15$ for $\theta' = 0$ and $\theta' = 0.2\pi$, respectively. (c) $N = 5$ photons in system size $L = 14 + 7$ with $\theta' = 0.1\pi$. The color scale is the number of pairs of adjacent occupied sites on the main chain (see text).

These oscillations can be attributed to photons from the bound-state hopping onto the extra sites and back. The towers appear as soon as $\theta' \neq 0$ and persist until approximately $\theta' \approx 0.3\pi$. The distance between the towers and therefore the oscillation frequency depends approximately linearly on θ'. Moreover, the shape and height of the towers depend on the number of decorations attached to the initially occupied sites.

Intriguingly, we find that the towers are more prominent for the five-photon initial bound state with two decorations on the second and fourth site [Fig. 16(c)] than for the state with three decorations on the first, third, and fifth site. Upon closer inspection, some towers of high-overlap states can also be discerned for $N = 3$ in Fig. 16(b). However, they are not as well differentiated as for $N = 5$, and do not appear to be equally spaced in energy, which is the reason why the oscillations in BSP at $\theta' = 0.2\pi$ are irregular, see Fig. 5(a). Interestingly, the towers do not become better resolved with increasing the photon number and the case of $N = 5$ actually features the sharpest towers and corresponding oscillations in BSP and various local observables, such as the number of photons in the extra sites. As a side note, similar looking towers of states are often found in systems that host "quantum many-body scars" [72–74], however, it is not clear whether similar physics occurs in the present case.

---

[1] I. Bloch, J. Dalibard, and W. Zwerger, Many-body physics with ultracold gases, Rev. Mod. Phys. **80**, 885 (2008).

[2] I. Bloch, J. Dalibard, and S. Nascimbène, Quantum simulations with ultracold quantum gases, Nat. Phys. **8**, 267 (2012).

[3] I. M. Georgescu, S. Ashhab, and F. Nori, Quantum simulation, Rev. Mod. Phys. **86**, 153 (2014).

[4] M. Kjaergaard, M. E. Schwartz, J. Braumüller, P. Krantz, J. I.-J. Wang, S. Gustavsson, and W. D. Oliver,

Superconducting qubits: Current state of play, Annu. Rev. Condens. Matter Phys. **11**, 369 (2020).

[5] R. Blatt and C. F. Roos, Quantum simulations with trapped ions, Nat. Phys. **8**, 277 (2012).

[6] A. A. Houck, H. E. Türeci, and J. Koch, On-chip quantum simulation with superconducting circuits, Nat. Phys. **8**, 292 (2012).

[7] C. Monroe, W. C. Campbell, L.-M. Duan, Z.-X. Gong, A. V. Gorshkov, P. W. Hess, R. Islam, K. Kim, N. M. Linke, G. Pagano, P. Richerme, C. Senko, and N. Y. Yao, Programmable quantum simulations of spin systems with trapped ions, Rev. Mod. Phys. **93**, 025001 (2021).

[8] A. Browaeys and T. Lahaye, Many-body physics with individually controlled Rydberg atoms, Nat. Phys. **16**, 132 (2020).

[9] A. Polkovnikov, K. Sengupta, A. Silva, and M. Vengalattore, *Colloquium*: Nonequilibrium dynamics of closed interacting quantum systems, Rev. Mod. Phys. **83**, 863 (2011).

[10] C. Gogolin and J. Eisert, Equilibration, thermalisation, and the emergence of statistical mechanics in closed quantum systems, Rep. Prog. Phys. **79**, 056001 (2016).

[11] L. D'Alessio, Y. Kafri, A. Polkovnikov, and M. Rigol, From quantum chaos and eigenstate thermalization to statistical mechanics and thermodynamics, Adv. Phys. **65**, 239 (2016).

[12] M. Ueda, Quantum equilibration, thermalization and prethermalization in ultracold atoms, Nat. Rev. Phys. **2**, 669 (2020).

[13] J. M. Deutsch, Quantum statistical mechanics in a closed system, Phys. Rev. A **43**, 2046 (1991).

[14] M. Srednicki, Chaos and quantum thermalization, Phys. Rev. E **50**, 888 (1994).

[15] M. Rigol, V. Dunjko, and M. Olshanii, Thermalization and its mechanism for generic isolated quantum systems, Nature **452**, 854 (2008).

[16] R. Nandkishore and D. A. Huse, Many-body localization and thermalization in quantum statistical mechanics, Annu. Rev. Condens. Matter Phys. **6**, 15 (2015).

[17] T. Kinoshita, T. Wenger, and D. S. Weiss, A quantum Newton's cradle, Nature **440**, 900 (2006).

[18] B. Sutherland, *Beautiful Models: 70 Years of Exactly Solved Quantum Many-Body Problems* (World Scientific, Singapore, 2004).

[19] B. Bertini, F. Heidrich-Meisner, C. Karrasch, T. Prosen, R. Steinigeweg, and M. Žnidarič, Finite-temperature transport in one-dimensional quantum lattice models, Rev. Mod. Phys. **93**, 025003 (2021).

[20] D. Mattis, *The Theory of Magnetism Made Simple: An Introduction to Physical Concepts and to Some Useful Mathematical Methods, The Theory of Magnetism Made Simple: An Introduction to Physical Concepts and to Some Useful Mathematical Methods* (World Scientific, Singapore, 2006).

[21] H. Bethe, Zur theorie der metalle, Z. Phys. **71**, 205 (1931).

[22] M. Date and M. Motokawa, Spin-cluster resonance in $CoCl_2 \cdot 2H_2O$, Phys. Rev. Lett. **16**, 1111 (1966).

[23] J. B. Torrance and M. Tinkham, Excitation of multiple-magnon bound states in $CoCl_2 \cdot 2H_2O$, Phys. Rev. **187**, 595 (1969).

[24] R. Hoogerbeets, A. J. van Duyneveldt, A. C. Phaff, C. H. W. Swuste, and W. J. M. de Jonge, Evidence for magnon bound-state excitations in the quantum chain system (C6H11N3)CuCl3, J. Phys. C: Solid State Phys. **17**, 2595 (1984).

[25] M. Ganahl, E. Rabel, F. H. L. Essler, and H. G. Evertz, Observation of complex bound states in the spin-1/2 Heisenberg *XXZ* chain using local quantum quenches, Phys. Rev. Lett. **108**, 077206 (2012).

[26] D. Gobert, C. Kollath, U. Schollwöck, and G. Schütz, Real-time dynamics in spin-$\frac{1}{2}$ chains with adaptive time-dependent density matrix renormalization group, Phys. Rev. E **71**, 036102 (2005).

[27] D. Petrosyan, B. Schmidt, J. R. Anglin, and M. Fleischhauer, Quantum liquid of repulsively bound pairs of particles in a lattice, Phys. Rev. A **76**, 033606 (2007).

[28] S. Langer, F. Heidrich-Meisner, J. Gemmer, I. P. McCulloch, and U. Schollwöck, Real-time study of diffusive and ballistic transport in spin-$\frac{1}{2}$ chains using the adaptive time-dependent density matrix renormalization group method, Phys. Rev. B **79**, 214409 (2009).

[29] J. Ren and S. Zhu, Quench dynamics of entanglement in an open anisotropic spin-$\frac{1}{2}$ Heisenberg chain, Phys. Rev. A **81**, 014302 (2010).

[30] L. F. Santos and A. Mitra, Domain wall dynamics in integrable and chaotic spin-1/2 chains, Phys. Rev. E **84**, 016206 (2011).

[31] R. Steinigeweg, S. Langer, F. Heidrich-Meisner, I. P. McCulloch, and W. Brenig, Coherent spin-current oscillations in transverse magnetic fields, Phys. Rev. Lett. **106**, 160602 (2011).

[32] S. Langer, M. Heyl, I. P. McCulloch, and F. Heidrich-Meisner, Real-time energy dynamics in spin-$\frac{1}{2}$ Heisenberg chains, Phys. Rev. B **84**, 205115 (2011).

[33] R. G. Pereira, S. R. White, and I. Affleck, Exact edge singularities and dynamical correlations in spin-1/2 chains, Phys. Rev. Lett. **100**, 027206 (2008).

[34] R. G. Pereira, S. R. White, and I. Affleck, Spectral function of spinless fermions on a one-dimensional lattice, Phys. Rev. B **79**, 165113 (2009).

[35] J.-S. Caux and J. M. Maillet, Computation of dynamical correlation functions of Heisenberg chains in a magnetic field, Phys. Rev. Lett. **95**, 077201 (2005).

[36] J.-S. Caux, R. Hagemans, and J. M. Maillet, Computation of dynamical correlation functions of Heisenberg chains: The gapless anisotropic regime, J. Stat. Mech.: Theory Exp. **2005**, P09003 (2005).

[37] M. Kohno, Dynamically dominant excitations of string solutions in the spin-1/2 antiferromagnetic Heisenberg chain in a magnetic field, Phys. Rev. Lett. **102**, 037203 (2009).

[38] A. Shashi, L. I. Glazman, J.-S. Caux, and A. Imambekov, Nonuniversal prefactors in the correlation functions of one-dimensional quantum liquids, Phys. Rev. B **84**, 045408 (2011).

[39] A. Imambekov, T. L. Schmidt, and L. I. Glazman, One-dimensional quantum liquids: Beyond the Luttinger liquid paradigm, Rev. Mod. Phys. **84**, 1253 (2012).

[40] T. Fukuhara, P. Schauß, M. Endres, S. Hild, M. Cheneau, I. Bloch, and C. Gross, Microscopic observation of magnon bound states and their dynamics, Nature **502**, 76 (2013).

[41] M. Vanicat, L. Zadnik, and T. Prosen, Integrable Trotterization: Local conservation laws and boundary driving, Phys. Rev. Lett. **121**, 030606 (2018).

[42] M. Ljubotina, L. Zadnik, and T. Prosen, Ballistic spin transport in a periodically driven integrable quantum system, Phys. Rev. Lett. **122**, 150605 (2019).

[43] P. W. Claeys, J. Herzog-Arbeitman, and A. Lamacraft, Correlations and commuting transfer matrices in integrable unitary circuits, SciPost Phys. **12**, 007 (2022).

[44] Google Quantum AI and Collaborators, Formation of robust bound states of interacting photons, Nature (London) **612**, 240 (2022).

[45] I. L. Aleiner, Bethe ansatz solutions for certain periodic quantum circuits, Ann. Phys. **433**, 168593 (2021).

[46] M. Fishman, S. R. White, and E. M. Stoudenmire, The ITensor Software Library for tensor network calculations, SciPost Phys. Codebases, 4 (2022).

[47] M. L. Mehta, *Random Matrices* (Elsevier, Amsterdam, 2004), Vol. 142.

[48] N. Regnault and R. Nandkishore, Floquet thermalization: Symmetries and random matrix ensembles, Phys. Rev. B **93**, 104203 (2016).

[49] V. Oganesyan and D. A. Huse, Localization of interacting fermions at high temperature, Phys. Rev. B **75**, 155111 (2007).

[50] L. D'Alessio and M. Rigol, Long-time behavior of isolated periodically driven interacting lattice systems, Phys. Rev. X **4**, 041048 (2014).

[51] L. F. Santos and M. Rigol, Localization and the effects of symmetries in the thermalization properties of one-dimensional quantum systems, Phys. Rev. E **82**, 031130 (2010).

[52] F. Haake, *Quantum Signatures of Chaos*, Physics and astronomy online library (Springer, Heidelberg, 2001).

[53] E. J. Torres-Herrera and L. F. Santos, Dynamical manifestations of quantum chaos: correlation hole and bulge, Philos. Trans. R. Soc. London, Series A **375**, 20160434 (2017).

[54] B. Bertini, P. Kos, and T. Prosen, Exact spectral form factor in a minimal model of many-body quantum chaos, Phys. Rev. Lett. **121**, 264101 (2018).

[55] A. Chan, A. De Luca, and J. T. Chalker, Solution of a minimal model for many-body quantum chaos, Phys. Rev. X **8**, 041019 (2018).

[56] J. Šuntajs, J. Bonča, T. c. v. Prosen, and L. Vidmar, Quantum chaos challenges many-body localization, Phys. Rev. E **102**, 062144 (2020).

[57] R. E. Prange, The spectral form factor is not self-averaging, Phys. Rev. Lett. **78**, 2280 (1997).

[58] M. Schiulaz, E. J. Torres-Herrera, F. Pérez-Bernal, and L. F. Santos, Self-averaging in many-body quantum systems out of equilibrium: Chaotic systems, Phys. Rev. B **101**, 174312 (2020).

[59] L. Colmenarez, D. J. Luitz, I. M. Khaymovich, and G. De Tomasi, Subdiffusive Thouless time scaling in the Anderson model on random regular graphs, Phys. Rev. B **105**, 174207 (2022).

[60] J. H. Robertson, R. Senese, and F. H. L. Essler, Decay of long-lived oscillations after quantum quenches in gapped interacting quantum systems, arXiv e-prints arXiv:2307.04466 [cond-mat.stat-mech] (2023).

[61] S. Scopa, P. Calabrese, and A. Bastianello, Entanglement dynamics in confining spin chains, Phys. Rev. B **105**, 125413 (2022).

[62] G. Zisling, L. F. Santos, and Y. B. Lev, How many particles make up a chaotic many-body quantum system?, SciPost Phys. **10**, 088 (2021).

[63] M. Kormos, M. Collura, G. Takács, and P. Calabrese, Real-time confinement following a quantum quench to a non-integrable model, Nat. Phys. **13**, 246 (2017).

[64] C.-J. Lin and O. I. Motrunich, Quasiparticle explanation of the weak-thermalization regime under quench in a nonintegrable quantum spin chain, Phys. Rev. A **95**, 023621 (2017).

[65] K. Hódsági, M. Kormos, and G. Takács, Quench dynamics of the Ising field theory in a magnetic field, SciPost Phys. **5**, 027 (2018).

[66] A. J. A. James, R. M. Konik, and N. J. Robinson, Nonthermal states arising from confinement in one and two dimensions, Phys. Rev. Lett. **122**, 130603 (2019).

[67] N. J. Robinson, A. J. A. James, and R. M. Konik, Signatures of rare states and thermalization in a theory with confinement, Phys. Rev. B **99**, 195108 (2019).

[68] S. Birnkammer, A. Bastianello, and M. Knap, Prethermalization in one-dimensional quantum many-body systems with confinement, Nat. Commun. **13**, 7663 (2022).

[69] J. Vovrosh, R. Mukherjee, A. Bastianello, and J. Knolle, Dynamical hadron formation in long-range interacting quantum spin chains, PRX Quantum **3**, 040309 (2022).

[70] S. Lu, M. C. Bañuls, and J. I. Cirac, Algorithms for quantum simulation at finite energies, PRX Quantum **2**, 020321 (2021).

[71] F. M. Surace and O. Motrunich, Robustness and eventual slow decay of bound states of interacting microwave photons in the Google Quantum AI experiment, PRX Quantum **5**, 010317 (2024).

[72] M. Serbyn, D. A. Abanin, and Z. Papić, Quantum many-body scars and weak breaking of ergodicity, Nat. Phys. **17**, 675 (2021).

[73] S. Moudgalya, B. A. Bernevig, and N. Regnault, Quantum many-body scars and Hilbert space fragmentation: A review of exact results, Rep. Prog. Phys. **85**, 086501 (2022).

[74] A. Chandran, T. Iadecola, V. Khemani, and R. Moessner, Quantum many-body scars: A quasiparticle perspective, Annu. Rev. Condens. Matter Phys. **14**, 443 (2023).